

Assessing and improving reliability of neighbor embedding methods: a map-continuity perspective

Zhexuan Liu* Rong Ma^{†‡} Yiqiao Zhong*

October 23, 2024

Abstract

Visualizing high-dimensional data is an important routine for understanding biomedical data and interpreting deep learning models. Neighbor embedding methods, such as t-SNE, UMAP, and LargeVis, among others, are a family of popular visualization methods which reduce high-dimensional data to two dimensions. However, recent studies suggest that these methods often produce visual artifacts, potentially leading to incorrect scientific conclusions. Recognizing that the current limitation stems from a lack of data-independent notions of embedding maps, we introduce a novel conceptual and computational framework, LOO-map, that learns the embedding maps based on a classical statistical idea known as the leave-one-out. LOO-map extends the embedding over a discrete set of input points to the entire input space, enabling a systematic assessment of map continuity, and thus the reliability of the visualizations. We find for many neighbor embedding methods, their embedding maps can be intrinsically discontinuous. The discontinuity induces two types of observed map distortion: “overconfidence-inducing discontinuity,” which exaggerates cluster separation, and “fracture-inducing discontinuity,” which creates spurious local structures. Building upon LOO-map, we propose two diagnostic point-wise scores—perturbation score and singularity score—to address these limitations. These scores can help identify unreliable embedding points, detect out-of-distribution data, and guide hyperparameter selection. Our approach is flexible and works as a wrapper around many neighbor embedding algorithms. We test our methods across multiple real-world datasets from computer vision and single-cell omics to demonstrate their effectiveness in enhancing the interpretability and accuracy of visualizations.

Keywords— Data visualization, t-SNE, UMAP, leave-one-out, perturbation, manifold learning, clustering, discontinuity

1 Introduction

Data visualization plays a crucial role in modern data science, as it offers essential and intuitive insights into high-dimensional datasets by providing low-dimensional embeddings of the data. Classical methods for dimension reduction include principal component analysis (PCA) [1], multidimensional scaling [2], locally linear embedding [3], among others. For visualizing high-dimensional data, the last two decades have witnessed rising popularity of t-SNE [4] and UMAP [5], which are extensively used in, e.g., single-cell analysis [6, 7, 8] and feature interpretations for deep learning models [9, 10].

The neighbor embedding methods [11, 12] are a family of visualization methods, which include t-SNE, UMAP, and LargeVis [13] as popular examples, that determine embedding points directly by

*Department of Statistics, University of Wisconsin–Madison, Madison, WI, 53706, USA. Emails: zhexuan.liu2@wisc.edu, yiqiao.zhong@wisc.edu

[†]Department of Biostatistics, T.H. Chan School of Public Health, Harvard University, Boston, MA 02115, USA. Email: rongma@hsph.harvard.edu

[‡]Department of Data Science, Dana-Farber Cancer Institute, Boston, MA 02115, USA.

solving a complicated optimization algorithm to minimize the discrepancy between similarities of input data points and those of the corresponding low-dimensional points. Given input data $\mathbf{x}_1, \dots, \mathbf{x}_n$, a neighbor embedding algorithm \mathcal{A} computes the points $(\mathbf{y}_1, \dots, \mathbf{y}_n) = \mathcal{A}(\mathbf{x}_1, \dots, \mathbf{x}_n)$ in the 2D plane, aiming to preserve the essential structures of $\mathbf{x}_1, \dots, \mathbf{x}_n$. Due to the algorithmic complexity, \mathcal{A} is often used as a black-box visualization tool. This is very different from classical dimension reduction methods such as PCA, where a parametric mapping \mathbf{f}_θ is determined and any input point \mathbf{x} is embedded through $\mathbf{y} = \mathbf{f}_\theta(\mathbf{x})$. For neighbor embedding methods, in contrast, there is no clearly defined embedding map for the “embedding points” $\mathbf{y}_1, \dots, \mathbf{y}_n$.

Due to the lack of explicit embedding maps [14], neighbor embedding methods suffer from both conceptual and practical difficulties. For conceptual difficulties, there is no obvious sample-independent notion of embedding maps, since the embedding points $\mathbf{y}_1, \dots, \mathbf{y}_n$ depend on n input points $\mathbf{x}_1, \dots, \mathbf{x}_n$ collectively, which makes it challenging to understand the correspondence between an input point \mathbf{x}_i and an embedding point \mathbf{y}_i . Thus, it is unclear what structures the embedding points inherit from the input points, even in ideal settings where inputs are drawn from known distributions or simple manifolds.

For practical difficulties, it has been recently recognized that neighbor embedding methods often produce misleading results by creating severe distortion through the embedding maps and introducing spurious clusters in low-dimensional visualization [15, 16]. Moreover, neighbor embedding methods are sensitive to the choice of optimization algorithms [17], initialization schemes [18], and hyperparameters [18, 19], which may lead to inconsistent interpretations [20].

Some progress has been made, but significant challenges remain. On the theoretical side, insights have been obtained regarding embedding stages [19, 21, 22], force-based interpretations [23], and visualization quality [21, 22, 24]. On the practical side, schemes of robust initialization and hyperparameter selection have been proposed [6, 16, 25, 26, 27]. To enhance the faithfulness of neighbor embedding methods, multiple diagnostic quantities have been proposed [6, 16, 25, 26]. In particular, Johnson et al. [28] and Xia et al. [27] propose algorithms to detect embedding points with severe neighborhood distortion, whereas Sun et al. [29] propose a dynamic approach to assess visualization uncertainty. However, due to a limited understanding of the origins and nature of the observed artifacts, most existing diagnostic methods offer only partial solutions and rely on ad hoc fixes, sometimes even introducing new artifacts (Figure 7).

In this work, we propose a notion of embedding map—which we call LOO-map—induced by a given neighbor embedding method \mathcal{A} . LOO-map is a mapping in the classical sense and approximates the properties of \mathcal{A} around each embedding point. It is based on a classical strategy from statistics known as the leave-one-out (LOO) method, which posits that adding, deleting, or changing a single input point has negligible effects on the overall inferential results. Using LOO, we can decouple the pairwise interaction in the algorithm \mathcal{A} : we add a new input point \mathbf{x} to $\mathbf{x}_1, \dots, \mathbf{x}_n$ and freeze $\mathbf{y}_1, \dots, \mathbf{y}_n$ in the optimization problem, allowing only one free variable \mathbf{y} . We call the resulting minimizer $\mathbf{f}(\mathbf{x})$ the LOO-map, which satisfies the approximation $(\mathbf{y}_1, \dots, \mathbf{y}_n, \mathbf{f}(\mathbf{x})) \approx \mathcal{A}(\mathbf{x}_1, \dots, \mathbf{x}_n, \mathbf{x})$. By design, the LOO-map \mathbf{f} not only satisfies $\mathbf{f}(\mathbf{x}_i) \approx \mathbf{y}_i$ for all i 's, but also reveals the embedding point $\mathbf{f}(\mathbf{x})$ of a potential new input point \mathbf{x} . As such, LOO-map extends the mapping defined over the discrete input set $\{\mathbf{x}_1, \dots, \mathbf{x}_n\}$ to the entire input space.

LOO-map provides a unified framework for both understanding recognized issues such as distance distortion [16, 30], low stability [29], and lack of neighborhood preservation [16, 31], and uncovering novel insights such as embedding discontinuity. In our view, discontinuities of $\mathbf{f}(\mathbf{x})$ represent an extreme form of distortion that accompanies topological changes in the embedding space, e.g., connected clusters become separated and a uniform shape is broken into fractured pieces. In contrast, classical dimension reduction methods such as PCA do not suffer from map discontinuity since a continuous parametric map $\mathbf{f}_\theta(\mathbf{x})$ is constructed explicitly. In this regard, embedding discontinuity is an innate issue of the family of neighbor embedding methods.

Using LOO-map, we identify two types of observed distortion patterns, one affecting global properties of the embedding map and the other affecting local relationships. Both types of distortions are a consequence of discontinuities in $\mathbf{f}(\mathbf{x})$ and can cause topological changes of the embedding structures.

- **Overconfidence-inducing (OI) discontinuity.** Overlapping clusters or data mixtures in the input

space are embedded into well-separated clusters, which creates a misleading visual impression of over-confidence that there is less uncertainty in the datasets. This biased perception of uncertainty can, in turn, lead to overly confident scientific conclusions.

- **Fracture-inducing (FI) discontinuity.** Small spurious and artificial clusters form in the embedding space, even for non-clustered data. Unlike OI discontinuity, such spurious clusters are small, localized, and formed in arbitrary locations.

We propose two point-wise diagnostic scores, namely *perturbation scores* and *singularity scores*, to quantify the severity of the two types of map discontinuity at each embedding point. Our approach is flexible and works as a wrapper around many neighbor embedding algorithms (Supplementary file Section E.1) without requiring any label information. To illustrate the diagnostic scores, we provide two use cases: the first shows that perturbation scores detect out-of-distribution data (or data with distribution shift) in computer vision, and the second shows that singularity scores aid users in selecting hyperparameters in single-cell data analysis.

The proposed method is evaluated extensively on simulated datasets and multiple real-world datasets, including two benchmarking datasets from computer vision and four single-cell omics datasets (see Supplementary Table S1 for description). The R package implementing our proposed method is available at the GitHub repository:

<https://github.com/zhexuandliu/NE-Reliability-MapContinuity>.

2 Results

2.1 Overview of methods

We provide an overview of LOO-map and demonstrate the proposed two diagnostic scores (Figure 1).

First, we introduce a general diagnosis strategy for discerning and analyzing discontinuity structure for neighbor embedding methods (e.g., t-SNE, UMAP). Given input data points $\mathbf{x}_1, \dots, \mathbf{x}_n$ in a potentially high-dimensional space, e.g., attribute vectors or feature vectors, we run an embedding algorithm such as t-SNE that returns embedding points $\mathbf{y}_1, \dots, \mathbf{y}_n$ in the 2D embedding space. Internally, a neighbor embedding method solves an optimization problem involving $O(n^2)$ pairwise interaction terms between embedding points and yields embedding points $(\mathbf{y}_1, \dots, \mathbf{y}_n) = \mathcal{A}(\mathbf{x}_1, \dots, \mathbf{x}_n)$. The LOO strategy rests on the assumption that none of the interaction terms is dominant so that perturbing any single input point has negligible effects overall on the embedding points. We verify this assumption extensively on both simulated datasets and real datasets (Table 1, Supplementary Table S2, Methods A.1). The LOO strategy allows us to add a new input \mathbf{x} and optimize its corresponding \mathbf{y} while freezing existing embedding points $(\mathbf{y}_j)_{j \leq n}$, and as a result, LOO-map is determined by solving a smaller optimization problem with only $O(n)$ effective terms due to frozen pair interaction between other embedding points. We identify the discontinuity points of $\mathbf{f}(\mathbf{x})$ as the source of the observed distortions and artifacts.

Then, we devise two diagnostic quantities (scores) that help to quantitatively assess the quality of embedding points. Both scores are computed for each embedding point without requiring any label information (Figure 1a). The first quantity, namely the perturbation score, quantifies how much an embedding point \mathbf{y}_i moves when the input \mathbf{x}_i is moderately perturbed, which helps to probe discontinuity of $\mathbf{f}(\mathbf{x})$ from the input space. The second quantity, namely the singularity score, measures how sensitive an embedding point is to an infinitesimal input perturbation, thus providing insights into the $\mathbf{f}(\mathbf{x})$ at each specific location $\mathbf{x} = \mathbf{x}_i$. The two scores, as we will show below, are motivated by different considerations and reveal qualitatively distinct features of the visualizations (Figure 1b-d).

Finally, we demonstrate how our proposed scores can improve the reliability of neighbor embedding methods. Two additional use cases are provided in Sections 2.6 and 2.7. Consider the workflow in Figure 1a: we obtain high-dimensional features of image data from a deep learning model (e.g., ResNet-18 [32]) and use t-SNE to embed features into 2D points. We observe that a fraction of inputs with ambiguous (mixed) class membership are misleadingly embedded into well-separated clusters (Figure 1c),

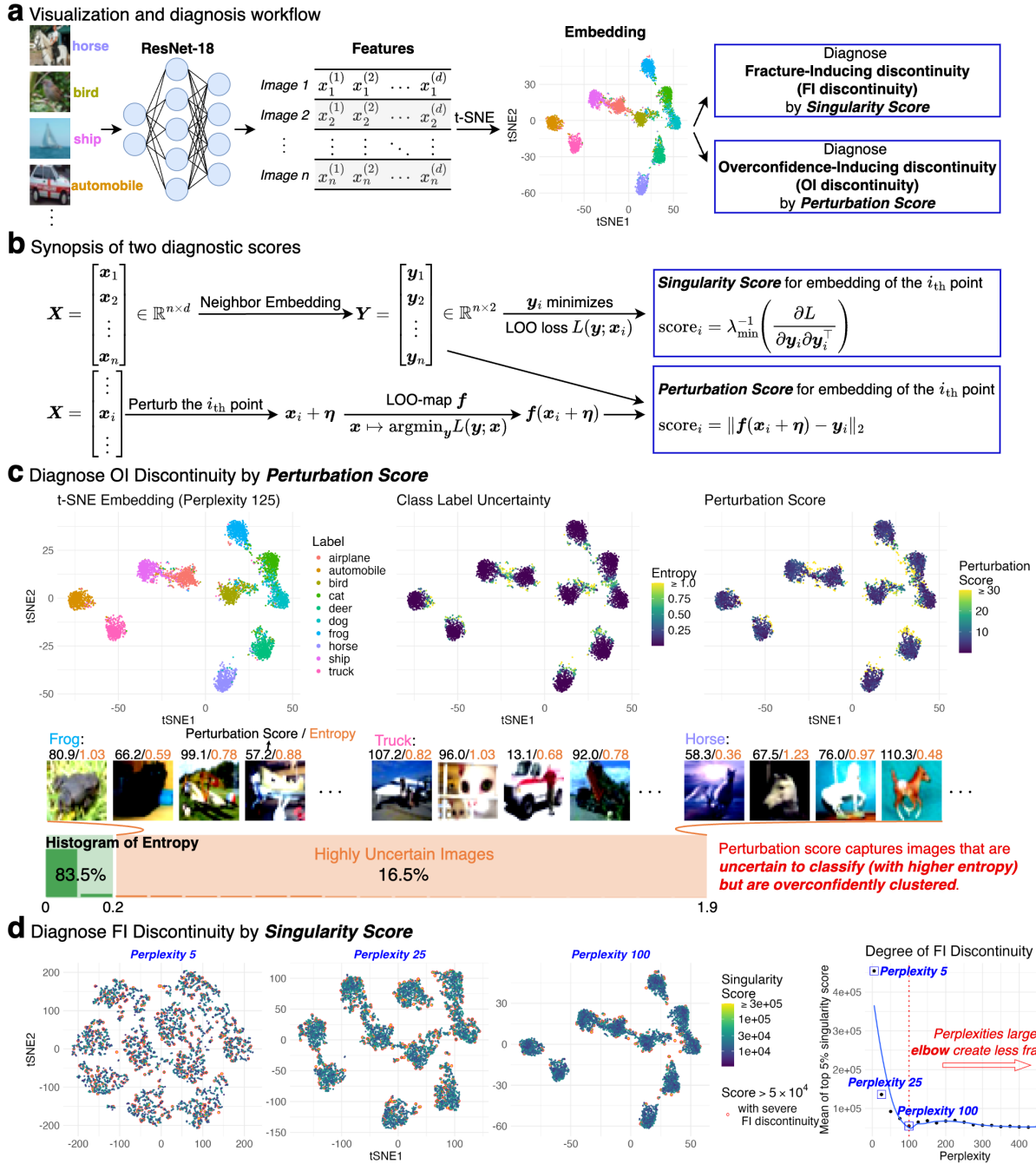


Figure 1: **Overview: assessment of embeddings by neighbor embedding methods with an example of image data.** **a** We use a standard pre-trained convolutional neural network (CNN) to obtain features of image samples from the CIFAR10 dataset, and then visualize the features using a neighbor embedding method, specifically t-SNE. **b** Basic ideas of singularity scores and perturbation scores. **c** t-SNE tends to embed image features into separated clusters even for images with ambiguous semantic meanings (as quantified by higher entropy of predicted class probabilities by the CNN). Perturbation scores identify the embedding points which have ambiguous class membership but less visual uncertainty. **d** Incorrect choice of the hyperparameter leads to visual fractures (FI discontinuity), which is more severe with a smaller perplexity. We recommend choosing the perplexity no smaller than the elbow point.

thereby creating overconfidence in the cluster structure. Indeed, both ground-truth class labels and label-informed entropy scores suggest that the visualization under-represents the uncertainty for mixed points, making them appear more distinct than they should be (Figure 1c, middle, right panels). Further examination of image examples confirms such an artifact of reduced uncertainty in the embedding space. As a diagnosis, we find that embedding points with high perturbation scores correlate well with such observed (OI) discontinuity.

Our second diagnostic scores can help hyperparameter selection. A practical challenge of interpreting t-SNE embeddings is that results may be sensitive to tuning parameters. Indeed, we find that a small perplexity tends to induce small and spurious structures similar to fractures visually, which suggests the presence of local (FI) discontinuity in the LOO-map f (Figure 1d). Our singularity score captures such FI discontinuity as more high-scoring points emerge under a smaller perplexity. With this diagnosis, we recommend choosing a perplexity no smaller than the elbow point of the FI discontinuity curve.

2.2 Leave-one-out as a general diagnosis technique

We start with a generic setup for neighbor embedding methods that encompasses SNE [33], t-SNE [4], UMAP [5], LargeVis [13], PaCMAP [15], among others. Let $\mathbf{X} = [\mathbf{x}_1, \dots, \mathbf{x}_n]^\top \in \mathbb{R}^{n \times d}$ be the input data matrix, and $\mathbf{Y} = [\mathbf{y}_1, \dots, \mathbf{y}_n]^\top \in \mathbb{R}^{n \times p}$ be the matrix of embedding points we aim to determine, where p can be 2 or 3. To find the embedding matrix \mathbf{Y} , we solve an optimization problem

$$\min_{\mathbf{y}_1, \dots, \mathbf{y}_n \in \mathbb{R}^2} \sum_{1 \leq i < j \leq n} \mathcal{L}(w(\mathbf{y}_i, \mathbf{y}_j); v_{i,j}(\mathbf{X})) + Z(\mathbf{Y}) \quad (1)$$

where $(v_{i,j})_{i < j}$ are the similarity scores calculated from $(\mathbf{x}_i)_{i \leq n} \in \mathbb{R}^d$ in the input space, and w is a function of embedding points $(\mathbf{y}_i)_{i \leq n}$ in the 2D or 3D space. The similarity scores $(v_{i,j})_{i < j}$ are often calculated based on a Gaussian kernel, and w takes the form of a heavy-tailed kernel. For example, in t-SNE algorithm (see Supplementary file Section E.2 for other neighbor embedding methods),

$$\begin{aligned} \mathcal{L}(w_{i,j}; v_{i,j}) &= -2v_{i,j} \log(w_{i,j}), \\ w_{i,j} = w(\mathbf{y}_i, \mathbf{y}_j) &= (1 + \|\mathbf{y}_i - \mathbf{y}_j\|^2)^{-1}, \quad Z(\mathbf{Y}) = \log \left(\sum_{k \neq l} w(\mathbf{y}_k, \mathbf{y}_l) \right). \end{aligned} \quad (2)$$

A fundamental challenge of assessing the embeddings is that we only know how *discrete points*—not the *input space*—are mapped, since the optimization problem is solved numerically by a complicated algorithm. Consequently, it is unclear if underlying structures (e.g., clusters, low-dimensional manifolds) in the input space are faithfully preserved in the embedding space.

Consider adding a new point \mathbf{x} to existing data points. We may wish to fix $\mathbf{x}_1, \dots, \mathbf{x}_n$ and analyze how embedding points $\mathcal{A}(\mathbf{x}_1, \dots, \mathbf{x}_n, \mathbf{x})$ change as we vary \mathbf{x} , thereby quantifying the mapping of \mathbf{x} under \mathcal{A} . As such, the embedding points would depend on all $n + 1$ input points.

LOO loss function and LOO-map. LOO is a generic decoupling technique that allows us to isolate the changes of one embedding point versus the others [34, 35, 36, 37, 38, 39]. Rooted in the *stability* idea [40, 41, 42], LOO assumes that adding (or deleting/modifying) a single input point does not change embedding points significantly (Figure 2a). This assumption allows us to study the map $\mathbf{x} \mapsto \mathcal{A}(\mathbf{x}_1, \dots, \mathbf{x}_n, \mathbf{x})$ approximately. Consider the optimization problem in Eqn. 1 with $n + 1$ inputs points $\mathbf{x}_1, \dots, \mathbf{x}_n, \mathbf{x}$ where we treat \mathbf{x} as the $(n + 1)$ -th point. Under the LOO assumption, when adding the new input point \mathbf{x} , we can freeze the embedding matrix $\mathbf{Y} = [\mathbf{y}_1, \dots, \mathbf{y}_n]^\top$ and allow only one free variable \mathbf{y} in the optimization problem. This simplification results in the LOO loss function defined by

$$L(\mathbf{y}; \mathbf{x}) = \sum_{1 \leq i \leq n} \mathcal{L} \left(w(\mathbf{y}_i, \mathbf{y}); v_{i,n+1} \left(\begin{bmatrix} \mathbf{X} \\ \mathbf{x}^\top \end{bmatrix} \right) \right) + Z \left(\begin{bmatrix} \mathbf{Y} \\ \mathbf{y}^\top \end{bmatrix} \right). \quad (3)$$

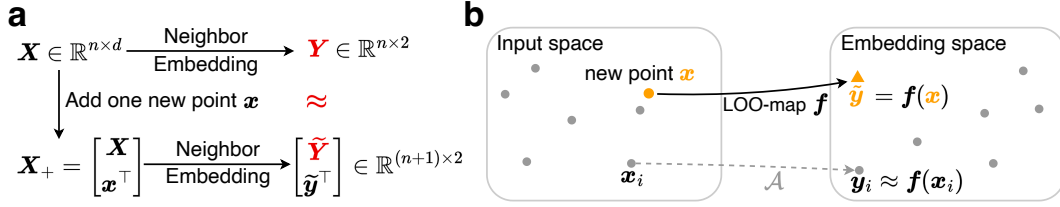


Figure 2: **Diagrams showing the idea of Leave-one-out (LOO) and LOO-map.** **a** Idea of LOO. Adding one input data does not significantly change the overall positions of embedding points. The assumption allows us to analyze the properties of the embedding map over the entire input space via an approximated loss which we call LOO loss. **b** We introduce a global embedding map (LOO-map) $f(x) = \operatorname{argmin}_{\mathbf{y}} L(\mathbf{y}; x)$ defined in the entire input space as an approximation to the neighbor embedding method \mathcal{A} .

We define the LOO-map as $f : x \mapsto \operatorname{argmin}_{\mathbf{y}} L(\mathbf{y}; x)$ (Figure 2b). The LOO loss is motivated by the following observation: suppose $\begin{bmatrix} \tilde{\mathbf{Y}} \\ \tilde{\mathbf{y}}^\top \end{bmatrix}$ is the embedding of $\mathbf{X}_+ = \begin{bmatrix} \mathbf{X} \\ \mathbf{x}^\top \end{bmatrix}$, i.e., it reaches the minimum of the original loss, then $\mathbf{y} = \tilde{\mathbf{y}}$ is necessarily the minimizer of a partial loss involving the embedding point of the added point x :

$$\begin{aligned} \tilde{\mathbf{y}} &= \operatorname{argmin}_{\mathbf{y} \in \mathbb{R}^2} \sum_{1 \leq i \leq n} \mathcal{L}\left(w(\tilde{\mathbf{y}}_i, \mathbf{y}); v_{i, n+1}\left(\begin{bmatrix} \mathbf{X} \\ \mathbf{x}^\top \end{bmatrix}\right)\right) + Z\left(\begin{bmatrix} \tilde{\mathbf{Y}} \\ \tilde{\mathbf{y}}^\top \end{bmatrix}\right) \\ &\approx \operatorname{argmin}_{\mathbf{y} \in \mathbb{R}^2} \sum_{1 \leq i \leq n} \mathcal{L}\left(w(\mathbf{y}_i, \mathbf{y}); v_{i, n+1}\left(\begin{bmatrix} \mathbf{X} \\ \mathbf{x}^\top \end{bmatrix}\right)\right) + Z\left(\begin{bmatrix} \mathbf{Y} \\ \mathbf{y}^\top \end{bmatrix}\right) \end{aligned}$$

where the approximation is based on the LOO assumption $\tilde{\mathbf{Y}} \approx \mathbf{Y}$. This approximation allows us to decouple the dependence of $\tilde{\mathbf{y}}_i$ on x .

Empirical validation of the LOO assumption. We empirically validate the LOO assumption by showing that \mathbf{Y} and $\tilde{\mathbf{Y}}$ are very close for large sample size n . Define the normalized error between embeddings before and after deleting a data point by

$$\epsilon_n = \frac{1}{\|\mathbf{Y}\|_F} \|\mathbf{Y} - \tilde{\mathbf{Y}}\|_F \quad (4)$$

where $\|\cdot\|_F$ means the Frobenius norm of a matrix. A sufficiently small ϵ_n will support the approximation in our derivation of the surrogate map. In implementation, due to the highly non-convex nature of the loss function, the embedding \mathbf{Y} is usually a local minimizer. We use this \mathbf{Y} as the initialization for the second run of the optimization algorithm to compute the new embedding $\tilde{\mathbf{Y}}$ (see Methods A.1).

We calculate this error extensively on both simulated and real datasets. The results support our LOO assumption (Table 1). We measured the approximation error ϵ_n across 20 independent trials and with different sample size n . We observe that the approximation errors are small and generally decreasing in n , which aligns with our LOO assumption. Methods A.1 details the experiment setup and Supplementary Table S2 contains comprehensive results in support of our LOO assumption.

2.3 LOO-map reveals intrinsic map discontinuities

By analyzing the LOO loss, we identify the two observed discontinuity patterns as a result of the map discontinuities of $f(x)$. We use t-SNE as an example to illustrate the main results.

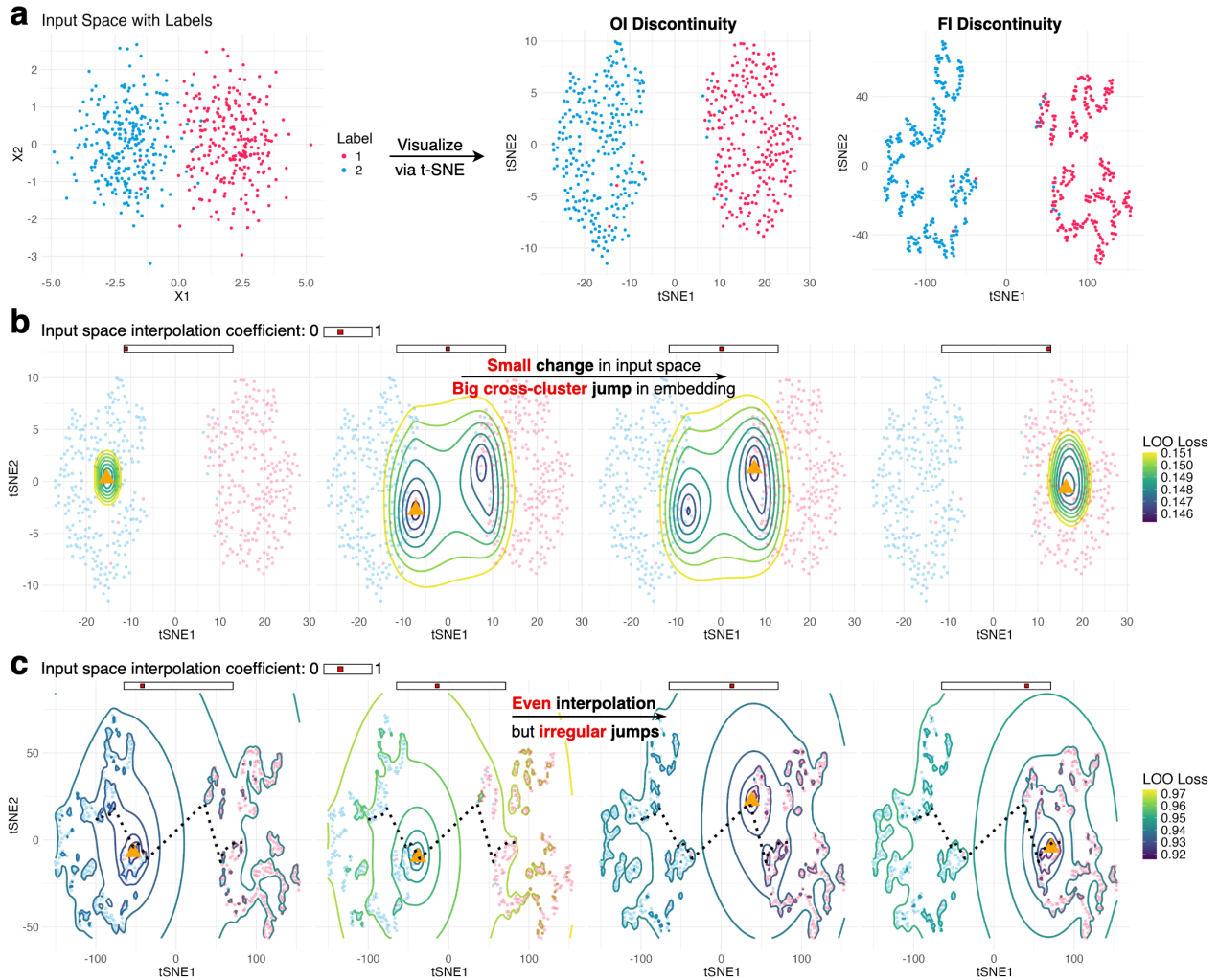


Figure 3: LOO loss landscape reveals the origins of two distortion patterns. **a** We illustrate two discontinuity patterns on simulated Gaussian mixture data. *OI discontinuity*: t-SNE embeds points into well-separated clusters and creates visual overconfidence. *FI discontinuity*: t-SNE with inappropriate perplexity creates many artificial fractures. **b** Origin of OI discontinuity: LOO loss contour plot shows distantly separated minima. We add a new input point \mathbf{x} at one of the 4 interpolated locations $\mathbf{x} = t\mathbf{c}_1 + (1-t)\mathbf{c}_2$ where $t \in \{0, 0.47, 0.48, 1\}$ and then visualize the landscape of the LOO loss $L(\mathbf{y}; \mathbf{x})$ respectively by contour plots. Middle plots exhibit two minima (orange triangle) in well-separated valleys, thus causing a huge jump of the embedding point (as minimizer of the LOO loss) under a small perturbation of \mathbf{x} . **c** Origin of FI discontinuity: We show LOO loss contour plots with interpolation coefficient $t \in \{0.2, 0.4, 0.6, 0.8\}$. The plots show many local minima and irregular jumps. Under an inappropriate perplexity, loss landscape is consistently fractured. Numerous local minima cause an uneven trajectory of embedding points (dashed line) when adding \mathbf{x} at evenly interpolated locations.

Number of points	$n = 1000$	$n = 3000$	$n = 5000$
2-GMM	0.068 (0.0017)	0.044 (0.0018)	0.034 (0.0007)
Swissroll	0.074 (0.0110)	0.043 (0.0041)	0.033 (0.0014)
CIFAR10	0.042 (0.0081)	0.044 (0.0013)	0.039 (0.0006)
IFNB	0.069 (0.0022)	0.049 (0.0019)	0.044 (0.0010)

Table 1: **Empirical validation of LOO on both simulated datasets and real datasets.** We measured the approximation error ϵ_n defined in Eqn. 4 across 20 independent trials and reported the average (and std) of ϵ_n . We find that the errors are small and generally decreasing in n , which supports our LOO assumption.

We generate mixture data by drawing $n = 500$ input points from two overlapping 2D Gaussian distributions. We run the t-SNE algorithm twice under perplexity 5 and 50 respectively—which are two representative choices for the key hyperparameter of t-SNE. The visualization plots confirm the existence of the two observed discontinuity patterns (Figure 3a). For OI discontinuity, the mixed points are embedded to the boundaries of two well-separated clusters, thereby creating misleadingly tight cluster structures. For FI discontinuity, the embedding points form fragmented small pieces, leading to many sub-clusters. Similar discontinuity patterns are also common among other neighbor embedding methods (Supplementary Figure S1).

We trace the origins of the observed discontinuity patterns by using the LOO loss function. To this end, we add a single point \mathbf{x} at varying locations to the input data and track how \mathbf{x} is mapped. By visualizing the landscape of the LOO loss function $L(\mathbf{y}; \mathbf{x})$ at four different inputs \mathbf{x} , we provide snapshots of the LOO-map $\mathbf{x} \mapsto \operatorname{argmin}_{\mathbf{y}} L(\mathbf{y}; \mathbf{x})$. More specifically, we choose the centers $\mathbf{c}_1, \mathbf{c}_2$ of the two Gaussian distributions and consider the interpolated input $\mathbf{x}(t) = t\mathbf{c}_1 + (1-t)\mathbf{c}_2$ where $t \in [0, 1]$. Since $\mathbf{x}(t)$ is mapped to the minimizer of the LOO loss, the loss valley reveals the trajectory of the corresponding embedding point $\mathbf{y}(t)$ under varying coefficients t .

We find that the observed OI discontinuity is caused by a discontinuity point of $\mathbf{f}(\mathbf{x})$ in the midpoint of two mixtures. To demonstrate this, we visualize the LOO loss landscape and the embedding of the added point $\mathbf{x}(t)$ at four interpolated locations where $t \in \{0, 0.47, 0.48, 1\}$. There are two clear well-separated valleys in the LOO loss landscape when $t \approx 0.5$ (Figure 3b). As a result, the embedding point $\mathbf{y}(t)$ jumps from one local minimum to the other minimum under a tiny change of t . A further gradient field analysis shows a hyperbolic geometry around the discontinuity point of $\mathbf{f}(\mathbf{x})$; see Section 2.10 for a mathematical description of the loss landscape.

We also find that the FI discontinuity is caused by numerous irregular local minima of $L(\mathbf{y}; \mathbf{x})$ under an inappropriate choice of perplexity. This conclusion is supported by the observation that the loss landscape of $L(\mathbf{y}; \mathbf{x})$ is consistently irregular and contains many local valleys under a small perplexity (Figure 3c). Moreover, varying the interpolation coefficient t from 0 to 1 at a constant speed results in an uneven trajectory of the embedding point $\mathbf{y}(t)$. Because of many irregularities, the embedding points tend to get stuck at these local minima, thus forming spurious sub-clusters. In addition, we find that larger perplexity typically lessens the severity of FI discontinuity (Supplementary Figure S2, S3).

2.4 LOO-map induces diagnosis scores for capturing topological changes

OI discontinuity and FI discontinuity reflect the properties of $\mathbf{f}(\mathbf{x})$ at two different levels: OI discontinuity is relatively global while FI discontinuity relatively local. To quantify the degree of discontinuity, we introduce two point-wise scores (see Methods A.2 for detailed definitions): (i) Perturbation scores capture the severity of OI discontinuity, and (ii) singularity scores capture the severity of FI discontinuity. For computational efficiency, both scores obtained are based on modifying individual embedding points instead of adding a new point so that we maintain n data points in total. This is justified by the LOO assumption that modifying/adding/deleting one point does not change embedding points much, allowing using the partial loss as LOO loss.

Briefly speaking, we define the i -th perturbation score as the change of an embedding point \mathbf{y}_i in the Euclidean distance under a perturbation of an input point \mathbf{x}_i of moderate length. As the data distribution is not known a priori, we search the perturbation directions using the top principal directions of the data (Methods A.2.1).

We define the i -th singularity score as the inverse of the smallest eigenvalue of a Hessian matrix that is related to the sensitivity of the embedding point \mathbf{y}_i under infinitesimal perturbation. Our derivation (Supplementary file Section E.1) indicates that small eigenvalues can cause significant local discontinuity, while a singular Hessian matrix leads to the sharpest discontinuity. We find infinitesimal perturbation well suited for capturing the local property of FI discontinuity. Detailed expressions for the singularity scores of t-SNE, UMAP and LargeVis are provided in Supplementary Section E.2.

Generally, we recommend using the perturbation score to diagnose the trustworthiness of cluster structures, and the singular score to detect spurious local structures.

2.5 Simulation studies

We implement our proposed point-wise scores for the t-SNE algorithm as an example and we believe that similar conclusions and results can be observed when applied to other neighbor embedding methods. We apply our diagnostic scores on two types of simulated datasets. (i) Gaussian mixture data (Methods A.4.1): we generate K centers $(\boldsymbol{\mu}_k)_{k=1}^K$ in the two-dimensional space, and then draw $n = 700$ input points with $K = 5$ and unequal mixture probabilities, and $n = 800$ input points with $K = 8$ and equal mixture probabilities. (ii) Swiss roll data (Methods A.4.2): we randomly generate $n = 800$ points from the Swiss-roll-shaped manifold in the three-dimensional space.

We apply perturbation scores to the 5-component Gaussian mixture data, where the t-SNE algorithm unfaithfully disperses the overlapping regions of the input data due to OI discontinuity, resulting in misleadingly distinct cluster boundaries in the embedding (Figure 4a left). Without any utilizing label information, our perturbation scores can identify the unreliable embedding points whose levels of uncertainty have been deceptively reduced by t-SNE (Figure 4a right). Meanwhile, the entropy difference uses the ground-truth labels to calculate the reduced class entropy (Methods A.3.2) in the embedding space, thus providing an objective evaluation of the degree of confidence (Figure 4a middle). Our perturbation scores align very well with entropy difference.

Next, we apply singularity scores to both the 8-component Gaussian mixture data and the Swiss roll data under two choices of perplexity (Figure 4b-c). For each embedding plot, we color points according to ground-truth information, singularity scores, and dichotomized singularity scores (namely converting to binary values with a threshold). We find that the embedding structures are visually different: a small perplexity creates many spurious sub-clusters while a large perplexity faithfully preserves the cluster structure and manifold structure of respective datasets. Moreover, the distribution of the dichotomized scores are qualitatively different: at a low perplexity many high-scoring embedding points are randomly located, while at a high perplexity there are fewer high-scoring embedding points.

Moreover, we provide further quantitative measurements of the clustering quality for the 8-component Gaussian mixture data based on three commonly used indices, namely DB index [43], within-cluster distance ratio (Methods A.3.4), and Wilks' Λ [44]. All three indices (small values are better) indicate that t-SNE visualizations with less severe FI discontinuity, i.e., lower singularity scores, achieve better clustering quality. In particular, DB index decreases from 0.7470 to 0.3821, within-cluster distance ratio decreases from 0.3625 to 0.1287, and Wilks' Λ decreases from 0.2244 to 0.0960. To further study the change in clustering quality, we generate 6 simulated datasets with varying cluster structures and dimensions. Across all datasets, we consistently observe an improvement in the clustering quality after tuning perplexity using the singularity scores: the DB index decreases by approximately 50% for each dataset, the within-cluster distance ratio decreases by 65%–91%, and Wilks' Λ decreases by 57%–99% after selecting a suitably larger perplexity (Supplementary Table S3).

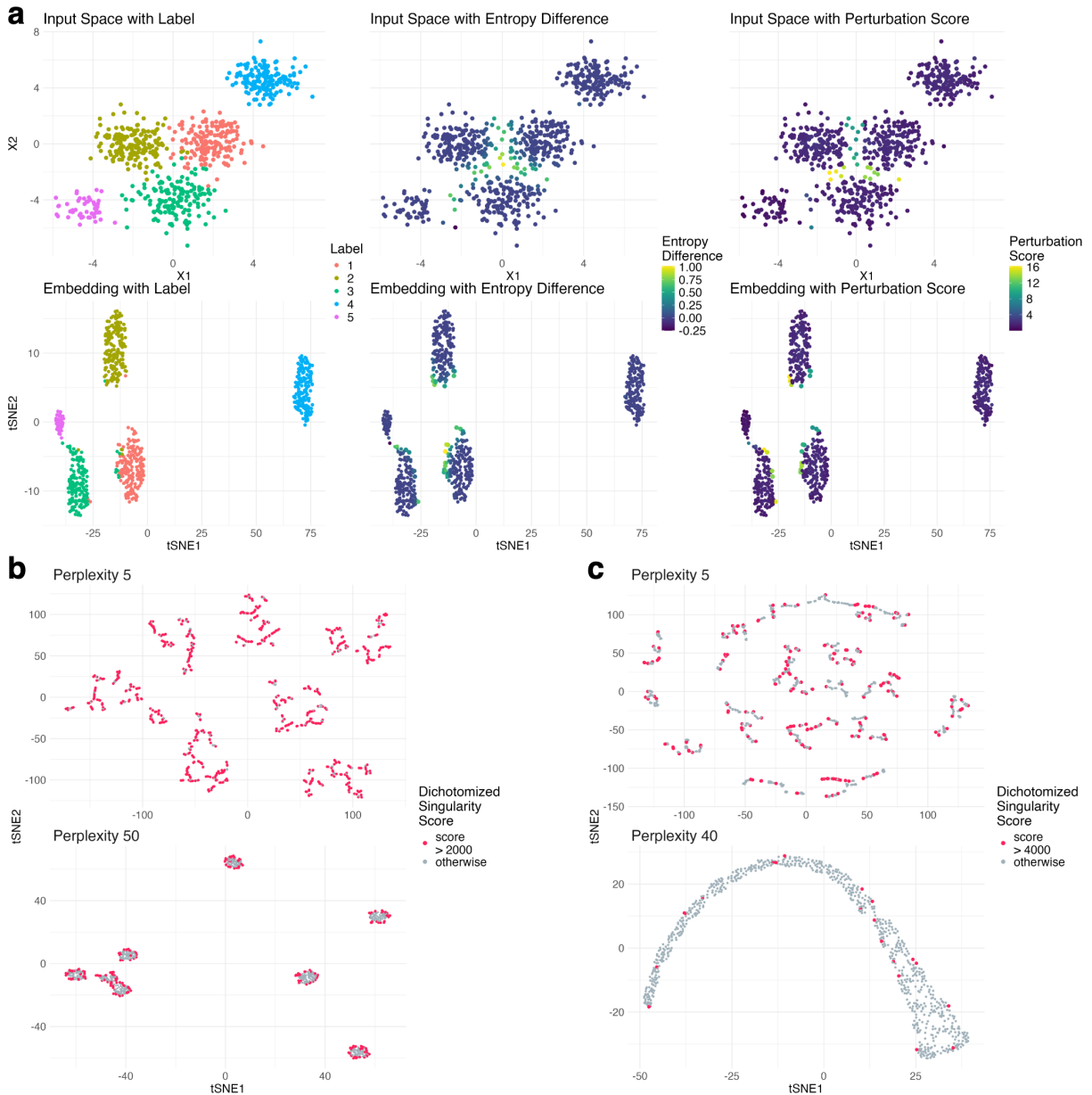


Figure 4: **Simulation studies demonstrate the effectiveness of proposed scores.** **a** Perturbation scores identify unreliable embedding points that have reduced uncertainty. Input points from 5-component Gaussian mixture data form separated clusters in the embedding space. t-SNE reduces perceived uncertainty for input points in the overlapping region (left), as captured by the label-dependent measurements entropy difference (middle). Our perturbation scores can identify the same unreliable embedding points without label information (right). **b-c** Singularity scores reveal spurious sub-clusters on Gaussian mixture data (**b**) and Swiss roll data (**c**). At a low perplexity, t-SNE creates many spurious sub-clusters. Embedding points receiving high singular scores at random locations are an indication of such spurious structure.

2.6 Use case 1: detecting out-of-distribution image data

One common practical issue for statistical methods or machine learning algorithms is *distribution shift*, where the training dataset and test dataset have different distributions, often because they are collected at different sources [45, 46, 47]. These test data are called out-of-distribution (OOD) data.

In this case study, we identify one rarely recognized pitfall of t-SNE visualization: OOD data may become harder to discern in t-SNE embeddings because they tend to be absorbed into other clusters. Our perturbation score is able to identify the dubious embedding points from OOD data.

We consider a standard ResNet-18 model [32, 48] trained on the CIFAR-10 dataset [49] as mentioned in Section 2.1. We use the model to extract features of CIFAR-10 test dataset as well as an OOD dataset known as DTD (describable textures dataset) [50]. Ideally, we hope that visualizing the features of test images and OOD images would reveal the distribution shift. However, the t-SNE embedding shows that a fraction of OOD features are absorbed into regular CIFAR-10 clusters that maintain tight cluster boundaries (Figure 5a). Without knowing the label information, one may mistakenly assume that the misplaced OOD embedding points belong to the regular and well-separated classes in CIFAR-10. We find that the OI discontinuity is the culprit of the embedding misplacement. Our inspection of the OOD features in the original space (before running the t-SNE algorithm) shows that misplaced OOD data points appear to have mixed membership, resembling both CIFAR-10 and OOD data—thus their cluster membership is in fact less certain than what t-SNE suggests.

Our perturbation scores can successfully identify most of these misplaced OOD embedding points (Figure 5b, c, d). The areas under the ROC curves (AUC) are on average 0.75 for the three selected clusters. Additionally, examining label prediction probabilities through the neural network reveals that the entropies of these probabilities are significantly correlated with the perturbation scores, with correlations of 0.49, 0.58, and 0.64 for the clusters shown in Figure 5b-d. These findings suggest that perturbation scores are effective in detecting OOD data and can help safeguard against misinterpretation of t-SNE visualizations.

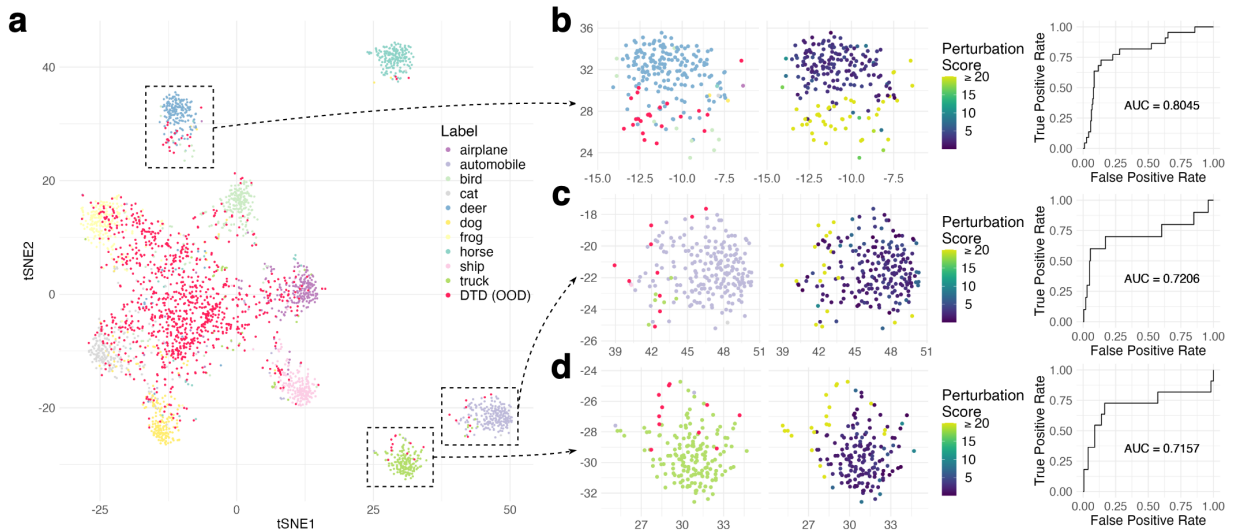


Figure 5: **Perturbation scores detect out-of-distribution (OOD) image data.** **a** We use pretrained ResNet-18 model to extract features of CIFAR-10 images and, as out-of-distribution data, of DTD texture images. Then we visualize the features using t-SNE. A fraction of OOD embedding points are absorbed into clusters that represent CIFAR-10 image categories such as deer, truck, and automobile. **b-d** Perturbation scores can effectively identify misplaced out-of-distribution data points. The ROC curves show the proportion of OOD points correctly identified by the perturbation scores.

2.7 Use case 2: enhancing interpretation of single-cell data

Our second example concerns the application of singularity scores in single-cell data. In this case study, we investigate how incorrect choices of perplexity induce spurious sub-clusters. We also provide a guide of choosing perplexity based on singularity scores, thereby reducing such spurious sub-clusters.

The first dataset we examined is a single-cell RNA-seq data of mouse embryonic stem cells (mESCs) undergoing differentiation [51]. This dataset contains the single-cell RNA sequencing data of 421 mouse embryonic stem cells collected at 5 sampling time points during differentiation. The second dataset is mouse brain single-cell ATAC-seq data [52]; this dataset records a collection of genome-wide chromatin accessibility profiles of 3618 mouse brain cells, summarized as the gene activity scores for each cell (Data Availability). These cells are labeled by 6 different cell type annotations. In our experiments, we vary a key tuning parameter in the t-SNE algorithm, namely perplexity. Briefly speaking, a higher perplexity means that input points have more “neighbors” in the calculation of similarity scores $v_{i,j}$.

Through analysis of both datasets, we find that a small perplexity tends to create spurious sub-clusters (Figure 6a, c). Our singular scores can provide informative insights into the spurious clusters even without the ground-truth labels, as summarized below.

1. (Distribution difference) Embedding points with large singularity scores tend to appear in random and scattered locations if the perplexity is too small. In contrast, under appropriate perplexity, embeddings with large singular scores are mostly in the periphery of clusters.
2. (Elbow point) As the perplexity increases, the magnitude of large singular scores (calculated as the average of the top 5%) rapidly decreases until the perplexity reaches a threshold.

The distribution of large singular values provides an informative indicator of the presence of spurious sub-clusters, which echoes the irregular landscape of the LOO loss function (Supplementary Figure S3a, c). We verified the distribution difference extensively using multiple statistical tests including Spearman’s rank correlation tests between singularity scores and distances to cluster centers, F-tests and permutation tests for a local regression model (singularity scores regressed against locations). We find that the p -values for all tests drop to a significant level after appropriately choosing the perplexity (Methods A.3.5). First, in the Spearman’s Rank correlation tests, at low perplexities, the correlations between singularity scores and locations are not significant in all five clusters in the mESCs data and all six clusters in the mouse brain ATAC data, with respective averaged p -values being 0.36 and 0.88 (after Holm-Bonferroni correction for multiple testing) (Supplementary Table S4). In contrast, after increasing the perplexities to the elbow points of the singularity score plots (Figure 6b,d), we observed significant correlations (at a significance level of 0.05) in four of five clusters in the mESCs data and three of six clusters in the mouse brain ATAC data. Next, for the F-tests and permutation tests for the local regression model, we tested whether the slope parameters in the local regression model are zero, and observed that p -values of both tests dropped from around 0.2 to less than 10^{-14} in the mESCs dataset and from around 0.09 to less than 10^{-15} in the mouse brain ATAC dataset, which indicated significant dependence of singularity scores on locations after increasing perplexity to the elbow points. The tests show that embedding points with high singularity scores transit from a disordered distribution at a low perplexity to an ordered distribution along the edges of clusters at a higher perplexity. Indeed, this location dependence can be explained by the geometry of LOO loss landscapes—a small perplexity may lead to many local minima in visually random locations (Supplementary Figure S3a, c) which then result in spurious sub-clusters, while a larger perplexity leads to more regular loss landscapes (Supplementary Figure S3b, d).

We also observe that the degree of FI discontinuity, as indicated by the magnitude of the singularity scores, decreases rapidly until the perplexity reaches the elbow point (Figure 6b, d). If we choose a perplexity larger than the elbow point, the spurious sub-clusters largely disappear from embeddings. This disappearance of sub-clusters is aligned with the improvement of neighborhood preservation (Figure 6b, d), as measured by the correlation of nearest-neighbor distances between the input space and the embedding space (Methods A.3.3). However, we would not suggest increasing perplexity excessively, as it may cause clusters to merge [25] and result in the loss of certain genuine local or microscopic structures [6].

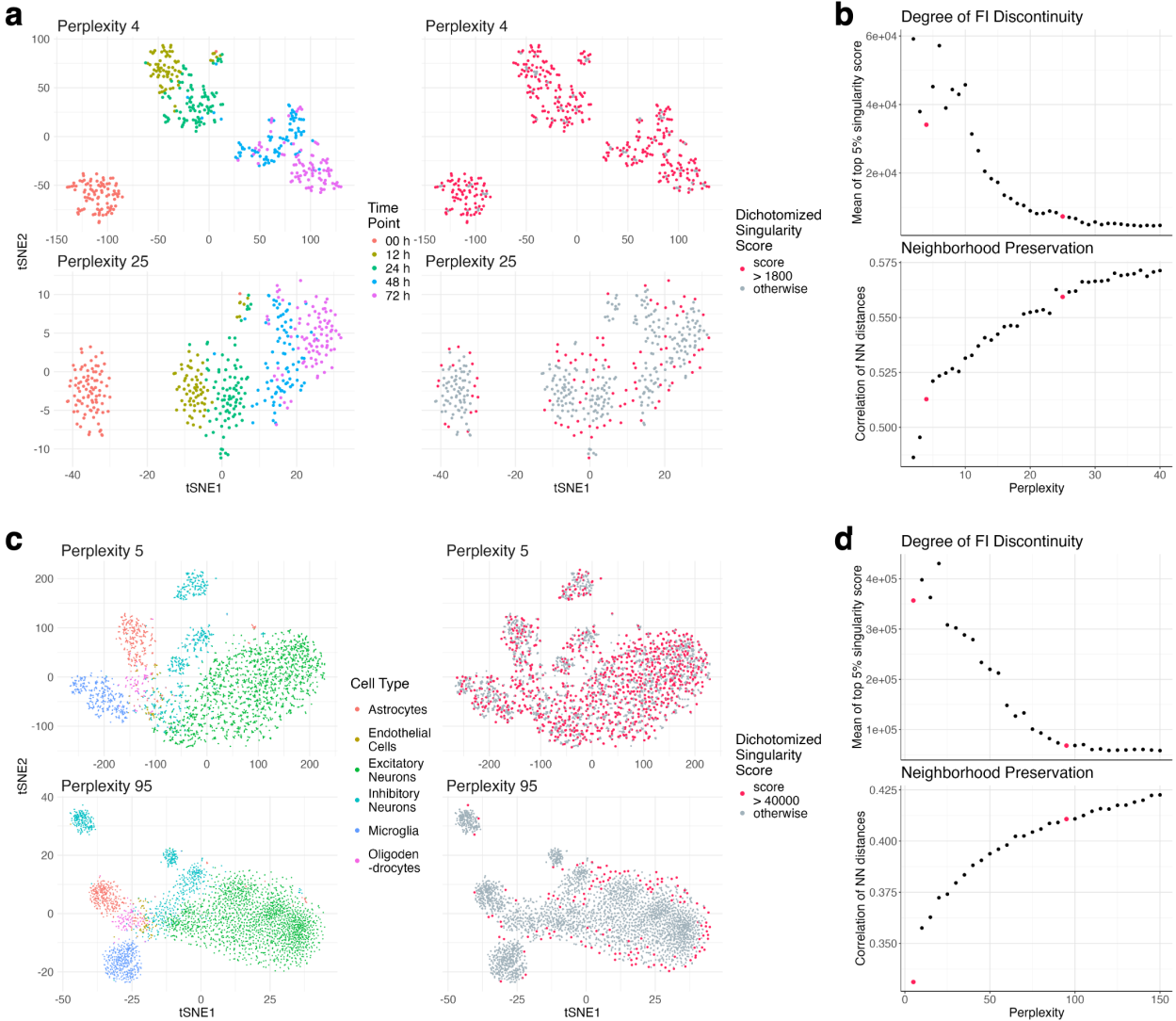


Figure 6: Singularity scores inform selection of the perplexity parameter. Comparative t-SNE embeddings and the corresponding singularity scores at two different perplexities in mouse embryonic cell differentiation data (**a**) and in mouse brain chromatin accessibility data (**c**). The tuning-parameter perplexity has a large impact on t-SNE visualization qualitatively. At small perplexity, there are many spurious sub-clusters. Embeddings with high singular scores appear in random locations, which indicate the presence of such spurious structures and severe FI discontinuity. Plots of degree of FI discontinuity and neighborhood preservation versus perplexity are shown for mouse embryonic cell differentiation data (**b**) and for mouse brain chromatin accessibility data (**d**). We recommend choosing perplexity no smaller than the elbow point, above which randomly located points with high singular scores disappear except in the peripheries of the clusters, and accordingly, the neighborhoods of most points are more faithfully embedded (better neighborhood preservation).

Also, a higher perplexity often leads to longer computational running time [26]. Therefore, we suggest choosing perplexity around the elbow point.

2.8 Computational costs

Perturbation score. The computational complexity for calculating the perturbation score per point is $O(n^2)$ flops, where the theoretical bottleneck lies in the calculation of similarity scores $(v_{i,j})_{i \leq j}$. Practically, our LOO loss has significantly sped up the evaluation of embedding points under perturbation by reducing the original optimization loss with $O(n^2)$ terms and $O(n)$ variables to $O(n)$ terms and $O(1)$ variables. Overall, it takes 35.2 seconds on a MacBook Air with Apple M2 chip to calculate the exact perturbation score per point for CIFAR-10 images in Figure 1.

We provide two optional methods in our R package as practical approximations to improve computation speed. First, we offer an approximation method which reduces the time of calculating perturbation scores to 7.1 seconds per point by reusing certain pre-computed quantities for approximation (Methods A.2.1). Second, we implement a pre-screening step to select a subset of the embedding points as the most likely high-scoring points, instead of calculating the scores for every point. We use the heuristics that high perturbation scores are often found at the peripheries of clusters. Such pre-screening of data points can significantly reduce computational effort while still providing a comparable assessment of OI discontinuity locations across the entire embedding (Supplementary Figure S5). Combining the two options leads to a reduction of running time by roughly 97%. In addition, since our perturbation scores are defined on a point-wise basis, they are highly parallelizable and can be further accelerated in computation.

Singularity score. The computational complexity for calculating the singularity scores for the entire dataset is $O(n^2)$ flops, primarily due to the matrix operations when calculating Hessian matrices.

Notably, the computation of singularity scores is relatively fast, requiring only 15.9 seconds in total on a MacBook Air with Apple M2 chip for a dataset with 5,000 points (Figure 1d). This fast speed is a desirable feature for tuning hyperparameters across multiple candidates. In addition, we expect further speedup in future improvements by exploiting the sparsity of similarity matrix at a low perplexity.

2.9 Comparison with other assessment metrics

There are multiple recent papers on assessing and improving the reliability of neighbor embedding methods. None of these papers view the observed artifacts as an intrinsic map discontinuity, and as a result, cannot reliably identify topological changes in their proposed diagnosis. For illustration, here we compare our method with EMBEDR [28], scDEED [27], and DynamicViz [29].

- **EMBEDR** identifies dubious points in an embedding by using statistical significance estimates as point-wise reliability scores. This process begins by computing point-wise KL divergences between the kernels in the input space and those in the embedding space, followed by a permutation test to determine whether the neighborhood preservation is significantly better than random chance. Lower p -values from the test indicate higher embedding reliability.
- **scDEED** calculates point-wise p -values by conducting a similar permutation test on the correlations of nearest-neighbor distances, in replace of KL divergences. Similarly, lower p -values indicate higher embedding reliability.
- **DynamicViz** employs a bootstrap approach to assess the stability of embeddings. A point-wise variance score is constructed based on resampling, defined as the mean variance of distances to the neighbors. Embedding points with lower variance scores are considered more reliable.

Both EMBEDR and scDEED focus on the faithfulness of neighborhood preservation. They treat the neighborhood structure of each point as a signal and test it against a randomized noisy baseline. However, neither methods aim to detect issues of topological changes and thus cannot accurately locate the discontinuity points. In contrast, our perturbation scores are designed to capture embedding points

that are close to the intrinsic discontinuity of the embedding maps. In this regard, perturbation scores are better at locating the changes of global structures.

We illustrate the advantages of our perturbation scores in identifying topological changes on a simulated Swiss roll dataset, where the t-SNE algorithm erroneously splits the smooth Swiss roll manifold into two disconnected pieces (Figure 7a). This visualization artifact represents a severe qualitative change: a smooth connected manifold is visualized as disconnected components, as reflected by the OI discontinuity. The perturbation scores unambiguously highlight the unreliable points exactly at the location where the disconnection occurs (Figure 7b). In comparison, both EMBEDR and scDEED evaluate most of the embedding points as unreliable and dubious, failing to identify the exact location of the discontinuity (Figure 7c, d).

In addition, while DynamicViz can roughly identify the location of the discontinuity (Figure 7e), it still fails to pinpoint the exact points where the split occurs due to the inherent variance in the bootstrap approach. Using a different dataset, we identify another limitation of DynamicViz. Specifically, the bootstrap procedure fails to robustly characterize the discontinuity locations in areas with lower point density, as these areas are prone to insufficient sampling (Supplementary Figure S7). In contrast, our perturbation scores are less susceptible to the low density regions.

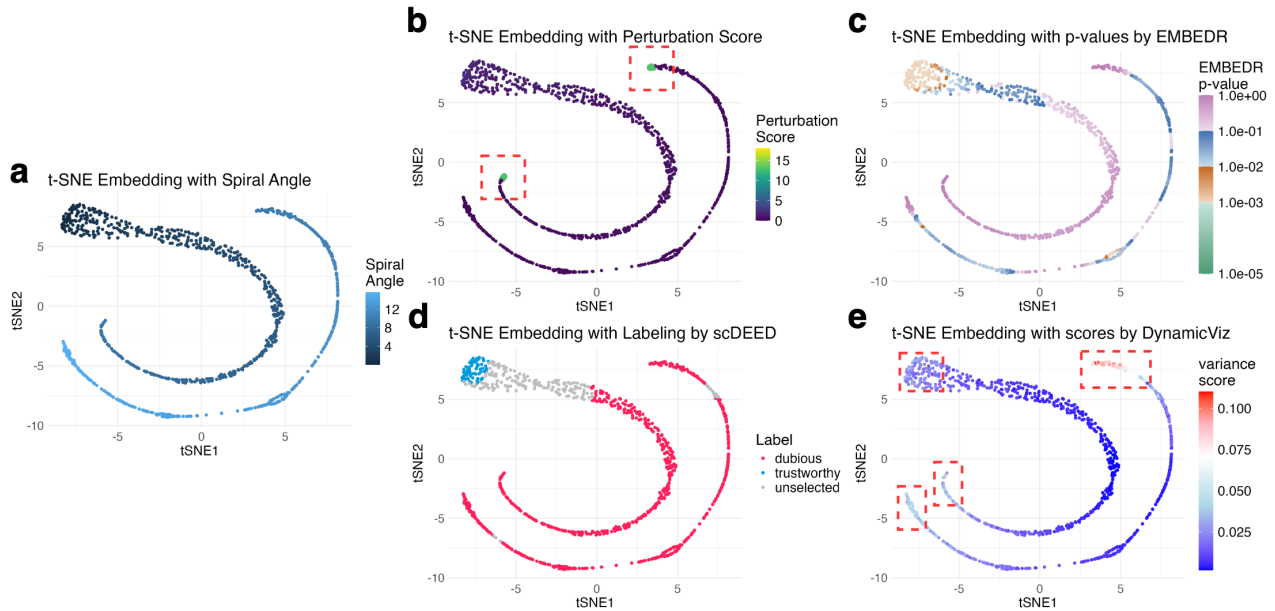


Figure 7: Comparing perturbation scores with three diagnostic scores for the t-SNE embedding on the simulated Swiss roll dataset. **a** t-SNE embedding of $n = 1000$ simulated points from the Swiss roll manifold. The colors correspond to the ground-truth spiral angles of the points. t-SNE algorithm erroneously breaks the smooth manifold into two disconnected parts, which indicates OI discontinuity. **b** Perturbation scores clearly mark the unreliable embedding points where disconnection (discontinuity) occurs. **c** EMBEDR suggests that most embedding points are unreliable (lower p -values are more reliable), but it does not identify the discontinuity location. **d** ScDEED evaluates most embedding points as dubious, but similar to EMBEDR, it does not identify the discontinuity location. **e** DynamicViz marks both the discontinuity location and the areas at both ends of the Swiss roll as unstable, making it difficult to distinguish the actual discontinuity locations. Furthermore, while it can roughly identify the discontinuity location, it still fails to pinpoint the exact points where the split occurs.

2.10 Theoretical insights: landscape of LOO loss

By analyzing the LOO loss function in Eqn. 3 under a simple setting, we will show that OI discontinuity is caused by a hyperbolic saddle point in the LOO loss function, thereby theoretically justifying Figure 3b.

Suppose that n input points x_1, \dots, x_n are generated from a data mixture with two well-separated and balanced groups, where the first group is represented by the index set $\mathcal{I}_+ \subset \{1, 2, \dots, n\}$ with $|\mathcal{I}_+| = n/2$ and the second group represented by $\mathcal{I}_- = \{1, 2, \dots, n\} \setminus \mathcal{I}_+$. Without loss of generality, we assume that the mean vectors of $(\mathbf{y}_i)_{i \in \mathcal{I}_+}$ and $(\mathbf{y}_i)_{i \in \mathcal{I}_-}$ are $\boldsymbol{\theta}$ and $-\boldsymbol{\theta}$ respectively, since embeddings are invariant to global shifts and rotations. Equivalently, we write

$$\mathbf{y}_i = \begin{cases} \boldsymbol{\theta} + \boldsymbol{\delta}_i & i \in \mathcal{I}_+ \\ -\boldsymbol{\theta} + \boldsymbol{\delta}_i & i \in \mathcal{I}_- \end{cases}$$

where $\sum_{i \in \mathcal{I}_+} \boldsymbol{\delta}_i = \sum_{i \in \mathcal{I}_-} \boldsymbol{\delta}_i = \mathbf{0}$. To simplify the loss function, we make an asymptotic assumption: consider (implicitly) a sequence of problems where input data have increasing distances between the two groups, so we expect increasing separation of clusters in the embedding space:

$$\|\boldsymbol{\theta}\| \rightarrow \infty, \quad \max_{i \leq n} \|\boldsymbol{\delta}_i\| = O(1).$$

Now considering adding an input point ('mixed' point) to a location close to the midpoint of the two groups. We assume that its similarity to the other inputs is

$$v_{i,n+1} = \begin{cases} p_0 + \varepsilon + o(\varepsilon) \\ p_0 - \varepsilon + o(\varepsilon) \end{cases}$$

for $1 \leq i \leq n$, where $p_0 > 0$ and ε is a small perturbation parameter. This assumption is reasonable because the similarity of the added point $\mathbf{x} = \mathbf{x}^\varepsilon$ has roughly equal similarities to existing inputs up to a small perturbation. We make the asymptotic assumption $\|\boldsymbol{\theta}\|^{-1} \asymp \varepsilon$, namely $\varepsilon\|\boldsymbol{\theta}\| = O(1)$ and $[\varepsilon\|\boldsymbol{\theta}\|]^{-1} = O(1)$.

Theorem 1. *Consider the LOO loss function for t -SNE given in Eqn. 3 and 2. Under the above stated assumptions, the negative gradient of the loss is*

$$-\nabla_{\mathbf{y}} L(\mathbf{y}; \mathbf{x}^\varepsilon) = (1 + o(1)) \left(\underbrace{\frac{\mathbf{y}_{\parallel} - \mathbf{y}_{\perp}}{\|\boldsymbol{\theta}\|^2}}_{\text{hyperbolic term}} + \underbrace{\frac{\varepsilon \boldsymbol{\theta}}{\|\boldsymbol{\theta}\|^2}}_{\text{perturbation term}} \right)$$

where $\mathbf{y}_{\parallel} = \boldsymbol{\theta}^\top \mathbf{y} / \|\boldsymbol{\theta}\|^2$ is projection of \mathbf{y} in the direction of $\boldsymbol{\theta}$, and $\mathbf{y}_{\perp} = \mathbf{y} - \mathbf{y}_{\parallel}$.

This result explains how the hyperbolic geometry creates OI discontinuity.

- The hyperbolic term indicates the unstable saddle point of the loss at $\mathbf{y} = \mathbf{0}$. Indeed, it is exactly the tangent vector of a hyperbola, so in the embedding force (negative gradient) field there is a pull force towards the x-axis and a push force away from the y-axis (Figure 8).
- The perturbation term reflects the effects of input point \mathbf{x}^ε . It tilts the negative gradients slightly in the direction of $\boldsymbol{\theta}$ if $\varepsilon > 0$ or $-\boldsymbol{\theta}$ if $\varepsilon < 0$, which causes the algorithm to jump between widely separated local minima of $L(\mathbf{y}; \mathbf{x})$ under small perturbations.

3 Discussion

In this paper, we developed a new framework for interpreting distortions in neighbor embedding methods as instances of map discontinuity by leveraging the LOO idea. Through our proposed LOO-map,

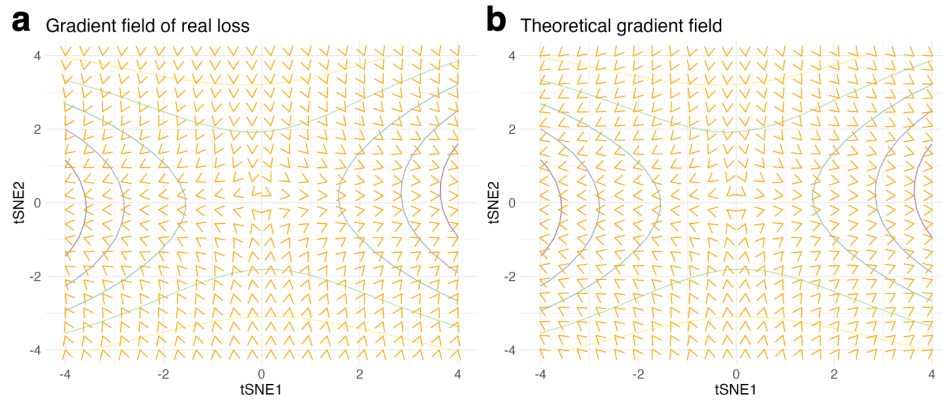


Figure 8: **Negative gradient fields of the real/theoretical LOO loss.** **a** We draw the negative gradient fields (force fields) $-\nabla_{\mathbf{y}}L(\mathbf{y}; \mathbf{x}^\varepsilon)$ based on the LOO loss under the same setting as in Figure 3b. **b** We draw a similar field plot based on the hyperbolic term $\frac{\mathbf{y} \cdot \mathbf{y}_\perp}{\|\boldsymbol{\theta}\|^2}$ from Theorem 1, where we take $\boldsymbol{\theta} = (\mathbf{c}_1 - \mathbf{c}_2)/2$ and $\mathbf{c}_1, \mathbf{c}_2$ are the centers of two clusters in the embedding. In addition, we add loss contours to both plots, which show hyperbolic paraboloids around the origin. We observe excellent alignment between the negative gradient field of the LOO loss and that of the theoretical analysis. Both field plots show a pull force towards the x-axis and a push force away from the y-axis.

we introduced two diagnostic scores aimed at identifying and addressing two distinct types of map discontinuities—OI and FI discontinuities. While our method has shown promising results, we acknowledge that our work may not account for all types of distortions. For example, factors such as initialization schemes, the choices of iterative algorithms, and other hyperparameters, may introduce different types of distortions. Additionally, we recognize the absence of a formal mathematical framework for rigorously characterizing the LOO-map.

In future research, we aim to establish connections between classical parametric embedding maps and the implicit embedding maps from neighbor embedding methods, which may fully address the topological issues and enhance both interpretability and faithfulness. One possible theoretical approach is [14]. Moreover, while our approach performs well on moderately sized datasets, further work is needed to develop scalable version of these methods. This includes developing more efficient optimization implementation, leveraging sparsity and tree-based approximation, and fully exploiting parallelism in computation.

A Methods

A.1 Verify Leave-one-out assumption empirically

Our LOO approach assumes that adding (or deleting/modifying) a single input point does not change the embeddings of other points on average significantly. To verify the LOO assumption, we conduct the following experiment.

Let $\mathbf{X} = [\mathbf{x}_1, \dots, \mathbf{x}_n]^\top$ be the input data matrix, and $\mathbf{Y} = [\mathbf{y}_1, \dots, \mathbf{y}_n]^\top$ be the matrix of embedding points. We then add one point \mathbf{x} to \mathbf{X} to have the new input data $\mathbf{X}_+ = [\mathbf{x}_1, \dots, \mathbf{x}_n, \mathbf{x}]^\top$. We then run t-SNE algorithm to obtain the embedding of \mathbf{X}_+ as $[\tilde{\mathbf{y}}_1, \dots, \tilde{\mathbf{y}}_n, \tilde{\mathbf{y}}]^\top$. Denoted $[\tilde{\mathbf{y}}_1, \dots, \tilde{\mathbf{y}}_n]$ as $\tilde{\mathbf{Y}}$. To verify LOO empirically, we keep track of the difference between \mathbf{Y} and $\tilde{\mathbf{Y}}$:

$$\epsilon_n = \frac{1}{\|\mathbf{Y}\|_F} \|\mathbf{Y} - \tilde{\mathbf{Y}}\|_F$$

and expect ϵ_n to be small.

We initialize the t-SNE algorithm in the second run by the embedding points we obtain from the first run: when calculating the embedding of \mathbf{X}_+ , we use \mathbf{Y} as the initialization for the first n points. This initialization scheme aims to address two issues: (i) the loss function in a neighbor embedding method is invariant to a global rotation and a global shift of all embedding points, so it is reasonable to choose embedding points with an appropriate initialization. (ii) There are potentially multiple local minima of the loss function due to non-convexity. We verify the LOO assumption at a given local minimum (namely \mathbf{Y}) obtained from the first run.

The experiment is conducted with different sample size n and with different types of dataset (simulated cluster data, simulated manifold data, real single-cell data, deep learning feature data). The comprehensive results showing the values of ϵ_n under different settings are presented in Supplementary Table S2. We observe that the approximation errors ϵ_n are small and generally decreasing in n , which supports our LOO assumption.

A.2 Two diagnosis scores

For implementation convenience, our calculation of the two diagnosis scores are based on modifying an input point instead of adding a new input point. According to the LOO assumption, the difference is negligible.

A.2.1 Perturbation score

Given an input data matrix $\mathbf{X} = [\mathbf{x}_1, \dots, \mathbf{x}_n]^\top$ and its embedding matrix $\mathbf{Y} = [\mathbf{y}_1, \dots, \mathbf{y}_n]^\top$, we view \mathbf{y}_i as the mapping of \mathbf{x}_i by the partial LOO-map \mathbf{f}_i :

$$\begin{aligned} \mathbf{f}_i(\mathbf{x}) &= \operatorname{argmin}_{\mathbf{y} \in \mathbb{R}^2} L_i(\mathbf{y}; \mathbf{x}), \quad \text{where} \\ L_i(\mathbf{y}; \mathbf{x}) &= \sum_{k \neq i} \mathcal{L}(w(\mathbf{y}_k, \mathbf{y}); v_{i,k}(\bar{\mathbf{X}})) + Z(\bar{\mathbf{Y}}). \end{aligned} \quad (5)$$

where $\bar{\mathbf{X}} = [\mathbf{x}_1, \dots, \mathbf{x}_{i-1}, \mathbf{x}, \mathbf{x}_{i+1}, \dots, \mathbf{x}_n]^\top$ differs from \mathbf{X} only at the i -th input point, and $\bar{\mathbf{Y}} = [\mathbf{y}_1, \dots, \mathbf{y}_{i-1}, \mathbf{y}, \mathbf{y}_{i+1}, \dots, \mathbf{y}_n]^\top$ has frozen embedding points except for the i -th point which is the decision variable in the optimization problem. This partial LOO-map \mathbf{f}_i is based on perturbing (or modifying) a single input point rather than adding a new point, thus maintaining n points in total. According to the LOO assumption, $\mathbf{f}_i \approx \mathbf{f}$, so we calculate perturbation score for the i -th point based on \mathbf{f}_i .

To assess the susceptibility of \mathbf{y}_i under moderate perturbation in \mathbf{x}_i , we apply a perturbation of length λ in the direction of \mathbf{e} to \mathbf{x}_i and measure the resulting change in mapping determined by the partial LOO-map \mathbf{f}_i . When implementing, we search the perturbation directions among the first 3 principal directions

of the data $\{e_1, e_2, e_3\}$ and their opposites $\{-e_1, -e_2, -e_3\}$, and the perturbation length λ is specified by the user. In this way, we can define the perturbation score of the i -th data point as

$$\max_{e \in \{\pm e_1, \pm e_2, \pm e_3\}} \|\mathbf{f}_i(\mathbf{x}_i + \lambda e) - \mathbf{y}_i\|_2. \quad (6)$$

In general, perturbation scores are not sensitive to perturbation length. Supplementary Figure S4 illustrates the perturbation scores of the CIFAR10 deep learning feature data for three perturbation lengths ($\lambda \in \{1, 2, 3\}$). Points with high perturbation scores remain consistent across different perturbation lengths. In practice, we recommend that users run perturbation score on a subset of data points and test with a few different perturbation lengths. Conceptually, the perturbation score detects points that fall within a radius of λ around the location of the OI discontinuity.

Moreover, we provide two approximation algorithms to accelerate the calculation of perturbation score for t-SNE along with a strategy for users to pre-screen points for which the perturbation score should be computed.

Approximation method 1. For high-dimensional input data, often PCA as a pre-processing step is implemented before calculating the similarity scores. As similarity scores are recalculated for each perturbation we consider, PCA is repeated numerous times, leading to a significant increase of computation. Since PCA is robust to perturbing a single input point, we reuse the pre-processed input points after one PCA calculation based on the original input data. This approximation avoids multiple calculation of PCA. We find that this approximation is sufficiently accurate, as the differences between perturbation scores by approximation method 1 and the exact perturbation scores are empirically negligible (Supplementary Figure S6a).

Approximation method 2. Besides reducing PCA computations, we can further accelerate the calculation of perturbation scores by approximating the similarity scores.

Given the input data matrix $\mathbf{X} = [\mathbf{x}_1, \dots, \mathbf{x}_n]^\top$ and perplexity \mathcal{P} , the computation of (exact) similarity scores $(v_{i,j}(\mathbf{X}))_{i < j}$ in the t-SNE algorithm follows the steps below.

1. Calculate the pairwise distance $d_{ij} = \|\mathbf{x}_i - \mathbf{x}_j\|_2$ for $i, j = 1, \dots, n$.
2. Find $\sigma_i, i = 1, \dots, n$ that satisfies

$$-\sum_{j \neq i} \frac{\exp(-d_{ij}^2/2\sigma_i^2)}{\sum_{k \neq i} \exp(-d_{ik}^2/2\sigma_i^2)} \log_2 \left(\frac{\exp(-d_{ij}^2/2\sigma_i^2)}{\sum_{k \neq i} \exp(-d_{ik}^2/2\sigma_i^2)} \right) = \log_2(\mathcal{P}). \quad (7)$$

3. Calculate $p_{j|i} = \frac{\exp(-d_{ij}^2/2\sigma_i^2)}{\sum_{k \neq i} \exp(-d_{ik}^2/2\sigma_i^2)}, i, j = 1, \dots, n$. And

$$v_{i,j}(\mathbf{X}) = \frac{p_{j|i} + p_{i|j}}{2n}.$$

The main computational bottleneck is at step 2, where we conduct binary search algorithm for n times to solve $(\sigma_i)_{1 \leq i \leq n}$.

To provide an approximation method, we note that when perturbing the k -th point, for $i \neq k$, Eqn. 7 still approximately holds for the original standard deviation σ_i since only one of the terms has been changed. Therefore, we can set $\tilde{\sigma}_i \approx \sigma_i$ for $i \neq k$ as an approximation to $(\tilde{\sigma}_i)_{1 \leq i \leq n}$, the standard deviations after perturbation. In this way, we only need to conduct the binary search once to solve $\tilde{\sigma}_k$, which significantly speeds up the calculation of the similarity scores after perturbation.

In terms of computational performance, approximation method 2 leads to a reduction of running time by nearly 80% for a dataset of size 5000. We also find that approximation method 2 is highly accurate. As shown in Supplementary Figure S6b, perturbation scores based on approximation method 2 are approximately equal to the exact perturbation scores for most of the points.

Pre-screening of points. To further speed up the computation, we use the heuristic that embedding points receiving high perturbation scores are often found at the peripheries of clusters. This heuristic motivates us to calculate the perturbation scores only for the peripheral points in the embedding space, since they are mostly likely the unreliable points. We find that applying this pre-screening step tends to find most of the unreliable points (Supplementary Figure S5) with significantly increased computational speed.

We use function `dbscan` in the R package `dbscan` (version 1.2-0) to identify embeddings on the periphery of clusters.

A.2.2 Singularity score

Given an input data matrix $\mathbf{X} = [\mathbf{x}_1, \dots, \mathbf{x}_n]^\top$ and its embedding matrix $\mathbf{Y} = [\mathbf{y}_1, \dots, \mathbf{y}_n]^\top$, we describe our derivation of singularity scores. If we add an infinitesimal perturbation $\epsilon \mathbf{e}$ to \mathbf{x}_i , then by the Taylor expansion of the partial LOO-map \mathbf{f}_i , the resulting change in the i -th embedding point is expressed as

$$\mathbf{f}_i(\mathbf{x}_i + \epsilon \mathbf{e}) - \mathbf{y}_i = -\epsilon \mathbf{H}_i^{-1} \sum_{k:k \neq i} \frac{\partial^2 \mathcal{L}(w(\mathbf{y}_i, \mathbf{y}_k); v_{i,k}(\mathbf{X}))}{\partial \mathbf{y}_i \partial \mathbf{x}_k^\top} \mathbf{e} + o(\epsilon), \quad (8)$$

where \mathbf{H}_i denote the Hessian matrix of the partial LOO loss $L_i(\mathbf{y}; \mathbf{x}_i)$ with respect to \mathbf{y} at $\mathbf{y} = \mathbf{y}_i$. Notably, when $\epsilon = 0$ (no perturbation), we have $\mathbf{f}_i(\mathbf{x}_i) = \mathbf{y}_i$. Denote the total loss as

$$\mathcal{L}(\mathbf{y}_1, \dots, \mathbf{y}_n; \mathbf{X}) = \sum_{1 \leq i < j \leq n} \mathcal{L}(w(\mathbf{y}_i, \mathbf{y}_j); v_{i,j}(\mathbf{X})) + Z(\mathbf{Y}).$$

Then, \mathbf{H}_i can be written as

$$\mathbf{H}_i = \left. \frac{\partial^2 L_i(\mathbf{y}; \mathbf{x}_i)}{\partial \mathbf{y} \partial \mathbf{y}^\top} \right|_{\mathbf{y}=\mathbf{y}_i} = \frac{\partial^2 \mathcal{L}(\mathbf{y}_1, \dots, \mathbf{y}_n; \mathbf{X})}{\partial \mathbf{y}_i \partial \mathbf{y}_i^\top},$$

i.e., \mathbf{H}_i also equals to the Hessian matrix of the total loss \mathcal{L} with respect to the i -th variable taking value at \mathbf{y}_i .

Importantly, \mathbf{H}_i is independent of the perturbation direction \mathbf{e} . The more singular \mathbf{H}_i is, the more sensitive the embedding point of \mathbf{x}_i becomes to infinitesimal perturbations. Thus, we define the singularity score of the i -th data point as the inverse of the smallest eigenvalue of the Hessian matrix of \mathcal{L} , that is $\lambda_{\min}^{-1}(\mathbf{H}_i)$. Supplementary file Section E.1 provides detailed derivations of Eqn. 8 and Supplementary file Section E.2 provides expressions of singularity scores for t-SNE, UMAP and LargeVis.

A.3 Scoring Metrics and Statistical Tests

A.3.1 Entropy of class probabilities

For a classification task, a statistical or machine learning algorithm outputs predicted class probabilities for a test data point. For example, in neural networks, the probabilities are typically obtained through a softmax operation in the final layer. Often, the model predicts a class with the largest probability among all classed. The entropy of the probabilities can quantify how confident the model is in its prediction.

For a classification task of k classes, if we denote the outputs class probabilities for one data point \mathbf{x} as $\mathbf{p} = (p_1, \dots, p_k)$, then we define the entropy as $E(\mathbf{p}) = -\sum_{j=1}^k p_j \log(p_j)$. This quantity is widely used for measuring the class uncertainty.

A.3.2 Entropy difference

We will describe an uncertainty measurement given access to the labels of input points. For a dataset $(\mathbf{x}_i)_{i \leq n}$ with clustering structures, we posit the following k -components Gaussian mixture model (GMM)

which each \mathbf{x}_i is sampled from. Consider a uniform prior on the k clusters, i.e., $p(A_j) = \frac{1}{k}$, $j = 1, 2, \dots, k$. Given cluster membership A_j , we define the conditional probability density function

$$p(\mathbf{x}|A_j) = g(\mathbf{x}|\boldsymbol{\mu}_j, \boldsymbol{\Sigma}_j),$$

where $\boldsymbol{\mu}_j, \boldsymbol{\Sigma}_j$ are the mean and covariance matrix in the j -th component, and $g(\mathbf{x}|\boldsymbol{\mu}_j, \boldsymbol{\Sigma}_j)$, $j = 1, 2, \dots, k$ are the Gaussian density functions with mean $\boldsymbol{\mu}_j$ and covariance matrix $\boldsymbol{\Sigma}_j$. We then have the posterior probability of A_j given an observation \mathbf{x} as

$$p(A_j|\mathbf{x}) = \frac{p(\mathbf{x}|A_j)}{\sum_{j=1}^k p(\mathbf{x}|A_j)}. \quad (9)$$

In the analysis of neighbor embedding methods, we will use the posterior probabilities as an uncertainty measurement. Given the ground-truth labels of the data points, we can fit two GMMs, one in the input space and the other in the embedding space, yielding estimated parameters $(\boldsymbol{\mu}_j, \boldsymbol{\Sigma}_j)_{j \leq k}$ for each fitted GMM. Then we can calculate the posterior probabilities of each data point belonging to the k components by Eqn. 9 with fitted parameters, in both the input space and the embedding space. For any data point, denote the posterior probabilities in input space as $\mathbf{p} = (p_1, p_2, \dots, p_k)$ and in embedding space as $\mathbf{q} = (q_1, q_2, \dots, q_k)$. Finally, we define the entropy difference for each point as the difference between the entropy of \mathbf{p} and the entropy of \mathbf{q} , i.e., $E(\mathbf{p}) - E(\mathbf{q}) = -\sum_{j=1}^k p_j \log(p_j) + \sum_{j=1}^k q_j \log(q_j)$.

The entropy difference measures the decreased uncertainty of cluster membership. A positive entropy difference means $E(\mathbf{q}) < E(\mathbf{p})$, so the associated data point appears to be less ambiguous in cluster membership after embedding. Vice versa, a negative entropy difference means increased uncertainty of a data point.

Since calculating entropy differences is based on the ground-truth labels and fitting a clear statistical model, we believe that entropy differences are a relatively objective evaluation of visual uncertainty. If a diagnosis score without label information is aligned with the entropy difference, then the diagnosis score is likely to be reliable.

A.3.3 Evaluation score of neighborhood preservation

We calculate point-wise neighborhood preservation scores to evaluate how well the local structures are preserved by an embedding algorithm. Given the input matrix \mathbf{X} and the embedding matrix \mathbf{Y} , to calculate the neighborhood preservation score for the i -th point, we first identify its k -nearest neighbors in the input space, with their indices denoted as $\mathcal{N}_i = \{i_1, i_2, \dots, i_k\}$. Then, we compute the distances from the i -th point to its neighbors in both the input and embedding spaces:

$$\begin{aligned} \mathbf{d}_i^{\text{input}} &= [d(\mathbf{x}_i, \mathbf{x}_{i_1}), \dots, d(\mathbf{x}_i, \mathbf{x}_{i_k})]^\top \\ \mathbf{d}_i^{\text{embedding}} &= [d(\mathbf{y}_i, \mathbf{y}_{i_1}), \dots, d(\mathbf{y}_i, \mathbf{y}_{i_k})]^\top. \end{aligned}$$

The neighborhood preservation score for the i -th point is defined as the correlation between $\mathbf{d}_i^{\text{input}}$ and $\mathbf{d}_i^{\text{embedding}}$. A higher correlation indicates better preservation of the neighborhood structure.

We use the median neighborhood preservation score across all points in the dataset to assess the overall neighborhood preservation of the embedding. For hyperparameters, we choose $k = \lceil n/5 \rceil$ and use the Euclidean distance as the metric d in implementation.

A.3.4 Indices and metrics for evaluating clustering quality

Davies-Bouldin Index. We calculate the DB index [43] using the R function `index.DB` in the R package `clusterSim` (version 0.51-3) with $p = q = 2$, i.e., using the Euclidean distance.

Within-cluster distance ratio. Consider m clusters and in each cluster i , there are n_i data points, denoted as $\{\mathbf{x}_{ij}\}_{1 \leq j \leq n_i}$. The centroid for each cluster is denoted as $\mathbf{x}_i = \frac{1}{n_i} \sum_{j=1}^{n_i} \mathbf{x}_{ij}$ and the mean of all data points is denoted as $\mathbf{x}_{..} = \frac{1}{n} \sum_{i=1}^m \sum_{j=1}^{n_i} \mathbf{x}_{ij}$.

Denote the total sum of squares (TSS) and within-cluster sum of squares (WSS) by

$$\text{TSS} = \sum_{i=1}^m \sum_{j=1}^{n_i} \|\mathbf{x}_{ij} - \mathbf{x}_{..}\|_2^2, \quad \text{WSS} = \sum_{i=1}^m \sum_{j=1}^{n_i} \|\mathbf{x}_{ij} - \mathbf{x}_i\|_2^2.$$

The within-cluster distance ratio is defined as $\text{WCDR} = \frac{\text{WSS}}{\text{TSS}}$. A smaller within-cluster distance ratio WCDCR indicates a more pronounced clustering effect.

Wilks' Λ . We compute Wilks' Λ statistic [44] by performing a multivariate analysis of variance using the `manova` function from the R package `stats` (version 4.2.1), followed by a statistical test.

A.3.5 Statistical tests for distribution difference of singularity scores

We have claimed that embedding points with large singularity scores tend to appear in random locations under small perplexities, but appear in the periphery of clusters under large perplexity. To quantitatively verify such distinction, we conduct several statistical tests and find that the results of the tests support our claim about the distribution difference (see Supplementary Table S4). We provide the details of the tests.

Tests for Spearman's rank correlation. Given the embedding $\mathbf{Y} = [\mathbf{y}_1, \dots, \mathbf{y}_n]^\top$ and the cluster label of each point as well as their singularity scores $\mathbf{s} = [s_1, \dots, s_n]^\top$, we can first calculate the distance of each point to its cluster center. The distance vector is denoted as $\mathbf{d} = [d_1, \dots, d_n]^\top$. We then conduct the Spearman's rank correlation test [53] on the singularity scores \mathbf{s} and the distances to cluster center \mathbf{d} . The tests shows that there is no significant correlation under low perplexity but significant correlation under larger perplexity (see p -values in Supplementary Table S4).

We use the function `cor.test` in the R package `stat` (version 4.2.1) to perform Spearman's rank correlation tests.

Tests for the local regression model. To test for distribution differences, we first fit a local regression model [54] using the singularity scores as the response variables and the coordinates of embedding points as predictors. Next, we fit a null model with the singularity scores as the response and only the intercept as the predictor. An F-test is then conducted to determine whether the magnitude of the singularity scores is associated with the locations of the embedding points.

We also perform permutation tests by shuffling the singularity scores and fitting a local regression model for each shuffle to approximate a null distribution for the residual sum of squares. Empirical p -values are then computed to assess whether the singularity scores are distributed randomly. Lower p -values suggest rejecting the null hypothesis of random distribution.

We use the `loess` function from the R package `stat` (version 4.2.1) to fit the local regression models.

A.4 Data processing

A.4.1 Gaussian mixture data

A Gaussian mixture model with k components is a linear combination of k component Gaussian densities. The probability density function of the random variable \mathbf{x} generated by Gaussian mixture model [55] is

$$p(\mathbf{x}|\boldsymbol{\lambda}) = \sum_{i=1}^k \pi_i g(\mathbf{x}|\boldsymbol{\mu}_i, \boldsymbol{\Sigma}_i),$$

where μ_i, Σ_i are the mean and covariance matrix in the i -th component, the scalars $\pi_i, i = 1, 2, \dots, k$ are the mixture weights satisfying $\sum_{i=1}^k \pi_i = 1$, and $g(x|\mu_i, \Sigma_i), i = 1, 2, \dots, n$ are the probability density functions of the Gaussian distribution family with mean μ_i and covariance matrix Σ_i .

We generated Gaussian mixture data using the function `rGMM` in the R package `MGMM` (version 1.0.1.1).

A.4.2 Swiss roll data

The Swiss roll data is a classical manifold data. Usually, the dataset consists of three-dimensional i.i.d. data points, denoted as $(x, y, z)^\top \in \mathbb{R}^3$, where

$$x = t \cos(t), y = t \sin(t), z = z.$$

Here, t is the parameter controlling the spiral angle and is uniformly distributed in a chosen range $[a, b]$. And z is the height parameter and is also uniformly distributed in the chosen span of heights $[c, d]$.

A.4.3 Deep learning feature data

We used the pretrained ResNet-18 model [48] to perform a forward pass on the CIFAR-10 test dataset to extract features of dimension 512. We also performed the forward pass using the same pre-trained model on the Describable Textures Dataset (DTD) dataset [50] as our out-of-distribution data in Section 2.6. We also randomly subsampled both datasets to reduce computational load. Specifically, in Section 1, we sampled 5000 images from the CIFAR-10 dataset as our deep learning feature data. In Section 2.6, we sampled 2000 CIFAR-10 images and 1000 DTD images, combining them into a dataset that includes OOD data points.

A.4.4 Mouse brain single-cell ATAC-seq data

The ATAC-seq datasets have been preprocessed by Luecken et al. ([52]). We applied the R functions `CreateSeuratObject`, `FindVariableFeatures` and `NormalizeData` in R package `Seurat` to identify 1000 most variable genes for 3618 cells. The dataset was subsampled when being used to verify the LOO assumption.

A.4.5 Mouse embryonic stem cell differentiation data

The single-cell RNA-seq data of mouse embryonic stem cells (mESCs) undergoing differentiation [51] were preprocessed, normalized, and scaled by following the standard procedures by R package `Seurat` using functions `CreateSeuratObject`, `NormalizeData` and `ScaleData`. We also used R function `FindVariableFeatures` to identify 2000 most variable genes for all 421 cells.

A.4.6 Human pancreatic tissue single-cell RNA-seq data

The single-cell RNA-seq data generated from human pancreatic tissues [56] were preprocessed, normalized, and scaled by following the standard procedures described above. We also used R function `FindVariableFeatures` to identify 2000 most variable genes for all 2364 cells. The dataset was subsampled when being used to verify the LOO assumption.

A.4.7 Single-cell RNA-seq data of PBMCs with treatment of interferon-beta

The single-cell RNA-seq data generated from PBMCs treated with interferon- β (IFNB) [57] were preprocessed, normalized, and scaled by following the standard procedures described above. We used R function `FindVariableFeatures` to identify 2000 most variable genes for all 6548 cells. The dataset was subsampled when being used to verify the LOO assumption.

A.5 Implementation of t-SNE

We used the function `Rtsne` in the R package `Rtsne` (version 0.17) to perform the t-SNE algorithm. We choose `theta = 0` to perform exact t-SNE. We also adjusted the code in `Rtsne` to access the similarity scores $(v_{i,j}(\mathbf{X}))_{i < j}$. The adjusted function `Rtsne` can be found in <https://github.com/zhexuandliu/NE-Reliability-MapContinuity>.

B Data availability

CIFAR-10 raw data is available from [49] [<https://www.cs.toronto.edu/kriz/cifar.html>]. Describable Textures Dataset is available from [50] [<https://www.robots.ox.ac.uk/vgg/data/dtd/>]. Mouse brain single-cell ATAC-seq data can be downloaded from Figshare (<https://figshare.com/ndownloader/files/25721789>). The ATAC-seq datasets have been preprocessed by Luecken et al. ([52]) to characterize gene activities. Mouse embryonic stem cell differentiation data is available in Gene Expression Omnibus with accession code [GSE98664]. The single-cell RNA-seq datasets generated from PBMCs treated with interferon- β and from human pancreatic tissues are available from R package `Seurat` (version 5.0.3) under the name “ifnb” and “panc8”, respectively. Source data are also provided.

C Code availability

The code for calculating the two diagnosis scores (as an R package), and the code for reproducing the simulation and analysis of this paper are available at <https://github.com/zhexuandliu/NE-Reliability-MapContinuity>.

D Acknowledgements

YZ is supported by NSF-DMS grant 2412052 and by the Office of the Vice Chancellor for Research and Graduate Education at the UW Madison with funding from the Wisconsin Alumni Research Foundation. ZL and YZ would like to thank Yixuan Li for suggesting out-of-distribution detection, and thank Sebastien Roch, Zexuan Sun, Xinyu Li and Jingyang Lyu for helpful discussions. RM would like to thank Jonas Fischer, Dmitry Kobak, Stefan Steinerberger and Bin Yu for helpful discussions on t-SNE and UMAP.

References

- [1] Pearson, K. On lines and planes of closest fit to systems of points in space. *The London, Edinburgh, and Dublin Philosophical Magazine and Journal of Science* **2**, 559–572 (1901). URL <https://doi.org/10.1080/14786440109462720>.
- [2] Torgerson, W. S. Multidimensional scaling: I. theory and method. *Psychometrika* **17**, 401–419 (1952). URL <https://doi.org/10.1007/BF02288916>.
- [3] Roweis, S. T. & Saul, L. K. Nonlinear dimensionality reduction by locally linear embedding. *Science* **290**, 2323–2326 (2000). URL <https://www.science.org/doi/pdf/10.1126/science.290.5500.2323>.
- [4] van der Maaten, L. & Hinton, G. Visualizing data using t-sne. *Journal of Machine Learning Research* **9**, 2579–2605 (2008). URL <http://jmlr.org/papers/v9/vandermaaten08a.html>.
- [5] McInnes, L., Healy, J. & Melville, J. Umap: Uniform manifold approximation and projection for dimension reduction (2020). URL <https://arxiv.org/abs/1802.03426>.
- [6] Kobak, D. & Berens, P. The art of using t-sne for single-cell transcriptomics. *Nature communications* **10**, 5416 (2019).
- [7] Linderman, G. C., Rachh, M., Hoskins, J. G., Steinerberger, S. & Kluger, Y. Fast interpolation-based t-sne for improved visualization of single-cell rna-seq data. *Nature methods* **16**, 243–245 (2019).
- [8] Luecken, M. D. & Theis, F. J. Current best practices in single-cell rna-seq analysis: a tutorial. *Molecular systems biology* **15**, e8746 (2019).
- [9] Jing, R., Xue, L., Li, M., Yu, L. & Luo, J. layerumap: A tool for visualizing and understanding deep learning models in biological sequence classification using umap. *iScience* **25**, 105530 (2022). URL <https://www.sciencedirect.com/science/article/pii/S2589004222018028>.
- [10] Islam, M. T. *et al.* Revealing hidden patterns in deep neural network feature space continuum via manifold learning. *Nature Communications* **14**, 8506 (2023). URL <https://doi.org/10.1038/s41467-023-43958-w>.
- [11] Assel, H. V., Espinasse, T., Chiquet, J. & Picard, F. A probabilistic graph coupling view of dimension reduction. In *Advances in Neural Information Processing Systems (NeurIPS)* (2022). URL https://proceedings.neurips.cc/paper_files/paper/2022/file/45994782a61bb51cad5c2bae36834265-Paper-Conference.pdf.
- [12] Agrawal, A., Ali, A. & Boyd, S. Minimum-distortion embedding. *Found. Trends Mach. Learn.* **14**, 211–378 (2021). URL <https://doi.org/10.1561/22000000090>.
- [13] Tang, J., Liu, J., Zhang, M. & Mei, Q. Visualizing large-scale and high-dimensional data. In *Proceedings of the 25th international conference on world wide web*, 287–297 (2016).
- [14] Auffinger, A. & Fletcher, D. Equilibrium distributions for t-distributed stochastic neighbour embedding (2023). URL <https://arxiv.org/abs/2304.03727>.
- [15] Wang, Y., Huang, H., Rudin, C. & Shaposhnik, Y. Understanding how dimension reduction tools work: An empirical approach to deciphering t-sne, umap, trimap, and pacmap for data visualization. *Journal of Machine Learning Research* **22**, 1–73 (2021). URL <http://jmlr.org/papers/v22/20-1061.html>.

- [16] Chari, T. & Pachter, L. The specious art of single-cell genomics. *PLOS Computational Biology* **19**, 1–20 (2023). URL <https://doi.org/10.1371/journal.pcbi.1011288>.
- [17] Yang, Z., Peltonen, J. & Kaski, S. Majorization-Minimization for Manifold Embedding. In *Proceedings of the Eighteenth International Conference on Artificial Intelligence and Statistics*, vol. 38 of *Proceedings of Machine Learning Research*, 1088–1097 (2015). URL <https://proceedings.mlr.press/v38/yang15a.html>.
- [18] Kobak, D. & Linderman, G. C. Initialization is critical for preserving global data structure in both t-sne and umap. *Nature Biotechnology* **39**, 156–157 (2021). URL <https://doi.org/10.1038/s41587-020-00809-z>.
- [19] Cai, T. T. & Ma, R. Theoretical foundations of t-sne for visualizing high-dimensional clustered data. *Journal of Machine Learning Research* **23**, 1–54 (2022). URL <http://jmlr.org/papers/v23/21-0524.html>.
- [20] The All of Us Research Program Genomics Investigators. Genomic data in the all of us research program. *Nature* **627**, 340–346 (2024). URL <https://doi.org/10.1038/s41586-023-06957-x>.
- [21] Arora, S., Hu, W. & Kothari, P. K. An analysis of the t-sne algorithm for data visualization. In *Proceedings of the 31st Conference On Learning Theory*, vol. 75 of *Proceedings of Machine Learning Research*, 1455–1462 (2018). URL <https://proceedings.mlr.press/v75/arora18a.html>.
- [22] Linderman, G. C. & Steinerberger, S. Clustering with t-sne, provably. *SIAM Journal on Mathematics of Data Science* **1**, 313–332 (2019). URL <https://doi.org/10.1137/18M1216134>.
- [23] Steinerberger, S. & Zhang, Y. t-sne, forceful colorings and mean field limits. *Research in the Mathematical Sciences* **9**, 42 (2022). URL <https://doi.org/10.1007/s40687-022-00340-4>.
- [24] Shaham, U. & Steinerberger, S. Stochastic neighbor embedding separates well-separated clusters (2017). URL <https://arxiv.org/abs/1702.02670>.
- [25] Wattenberg, M., Viégas, F. & Johnson, I. How to use t-sne effectively. *Distill* (2016). URL <http://distill.pub/2016/misread-tsne>.
- [26] Belkina, A. C. *et al.* Automated optimized parameters for t-distributed stochastic neighbor embedding improve visualization and analysis of large datasets. *Nature Communications* **10**, 5415 (2019). URL <https://doi.org/10.1038/s41467-019-13055-y>.
- [27] Xia, L., Lee, C. & Li, J. J. Statistical method sceed for detecting dubious 2d single-cell embeddings and optimizing t-sne and umap hyperparameters. *Nature Communications* **15**, 1753 (2024). URL <https://doi.org/10.1038/s41467-024-45891-y>.
- [28] Johnson, E. M., Kath, W. & Mani, M. Embedr: Distinguishing signal from noise in single-cell omics data. *Patterns* **3**, 100443 (2022). URL <https://www.sciencedirect.com/science/article/pii/S2666389922000162>.
- [29] Sun, E. D., Ma, R. & Zou, J. Dynamic visualization of high-dimensional data. *Nature Computational Science* **3**, 86–100 (2023). URL <https://doi.org/10.1038/s43588-022-00380-4>.
- [30] Zhou, Y. & Sharpee, T. O. Using Global t-SNE to Preserve Intercluster Data Structure. *Neural Computation* **34**, 1637–1651 (2022). URL https://doi.org/10.1162/neco_a_01504.

- [31] Cooley, S. M., Hamilton, T., Aragonés, S. D., Ray, J. C. J. & Deeds, E. J. A novel metric reveals previously unrecognized distortion in dimensionality reduction of scRNA-seq data. *bioRxiv* (2022). URL <https://www.biorxiv.org/content/early/2022/01/09/689851>.
- [32] He, K., Zhang, X., Ren, S. & Sun, J. Deep residual learning for image recognition. In *2016 IEEE Conference on Computer Vision and Pattern Recognition (CVPR)*, 770–778 (2016).
- [33] Hinton, G. E. & Roweis, S. Stochastic neighbor embedding. In *Advances in Neural Information Processing Systems (NeurIPS)* (2002). URL https://proceedings.neurips.cc/paper_files/paper/2002/file/6150ccc6069bea6b5716254057a194ef-Paper.pdf.
- [34] Quenouille, M. H. Notes on bias in estimation. *Biometrika* **43**, 353–360 (1956). URL <http://www.jstor.org/stable/2332914>.
- [35] Stone, M. Cross-Validatory Choice and Assessment of Statistical Predictions. *Journal of the Royal Statistical Society: Series B (Methodological)* **36**, 111–133 (1974). URL <https://doi.org/10.1111/j.2517-6161.1974.tb00994.x>.
- [36] Stone, M. An asymptotic equivalence of choice of model by cross-validation and akaike’s criterion. *Journal of the Royal Statistical Society: Series B (Methodological)* **39**, 44–47 (1977). URL <http://www.jstor.org/stable/2984877>.
- [37] Geisser, S. The predictive sample reuse method with applications. *Journal of the American Statistical Association* **70**, 320–328 (1975). URL <http://www.jstor.org/stable/2285815>.
- [38] Craven, P. & Wahba, G. Smoothing noisy data with spline functions. *Numerische Mathematik* **31**, 377–403 (1978). URL <https://doi.org/10.1007/BF01404567>.
- [39] Gene H. Golub, M. H. & Wahba, G. Generalized cross-validation as a method for choosing a good ridge parameter. *Technometrics* **21**, 215–223 (1979). URL <https://www.tandfonline.com/doi/abs/10.1080/00401706.1979.10489751>.
- [40] Breiman, L. Heuristics of instability and stabilization in model selection. *The Annals of Statistics* **24**, 2350 – 2383 (1996). URL <https://doi.org/10.1214/aos/1032181158>.
- [41] Breiman, L. Statistical Modeling: The Two Cultures (with comments and a rejoinder by the author). *Statistical Science* **16**, 199 – 231 (2001). URL <https://doi.org/10.1214/ss/1009213726>.
- [42] Yu, B. Stability. *Bernoulli* **19**, 1484 – 1500 (2013). URL <https://doi.org/10.3150/13-BEJSP14>.
- [43] Davies, D. L. & Bouldin, D. W. A cluster separation measure. *IEEE Transactions on Pattern Analysis and Machine Intelligence* **PAMI-1**, 224–227 (1979).
- [44] Wilks, S. S. Certain generalizations in the analysis of variance. *Biometrika* **24**, 471–494 (1932). URL <http://www.jstor.org/stable/2331979>.
- [45] Yang, J., Zhou, K., Li, Y. & Liu, Z. Generalized out-of-distribution detection: A survey. *International Journal of Computer Vision* (2024). URL <https://doi.org/10.1007/s11263-024-02117-4>.
- [46] Koh, P. W. *et al.* WILDS: A benchmark of in-the-wild distribution shifts. In *International Conference on Machine Learning (ICML)* (2021).

- [47] Zech, J. R. *et al.* Variable generalization performance of a deep learning model to detect pneumonia in chest radiographs: A cross-sectional study. *PLoS Medicine* **15**, 1–17 (2018). URL <https://doi.org/10.1371/journal.pmed.1002683>.
- [48] Dadalto, E. Resnet-18 model trained on cifar-10 (2023). URL https://huggingface.co/edadaltocg/resnet18_cifar10.
- [49] Krizhevsky, A. Learning multiple layers of features from tiny images. Tech. Rep., University of Toronto, Toronto, Ontario (2009). URL <https://www.cs.toronto.edu/~kriz/learning-features-2009-TR.pdf>.
- [50] Cimpoi, M., Maji, S., Kokkinos, I., Mohamed, S. & Vedaldi, A. Describing textures in the wild. In *2014 IEEE Conference on Computer Vision and Pattern Recognition*, 3606–3613 (2014).
- [51] Hayashi, T. *et al.* Single-cell full-length total rna sequencing uncovers dynamics of recursive splicing and enhancer rnas. *Nature Communications* **9**, 619 (2018). URL <https://doi.org/10.1038/s41467-018-02866-0>.
- [52] Luecken, M. D. *et al.* Benchmarking atlas-level data integration in single-cell genomics. *Nature Methods* **19**, 41–50 (2022).
- [53] Best, D. J. & Roberts, D. E. Algorithm as 89: The upper tail probabilities of spearman’s rho. *Journal of the Royal Statistical Society. Series C (Applied Statistics)* **24**, 377–379 (1975). URL <http://www.jstor.org/stable/2347111>.
- [54] Cleveland, W. S., Grosse, E. & Shyu, W. M. *Local Regression Models*, chap. 8, 309–376 (Wadsworth & Brooks/Cole, 1992).
- [55] Reynolds, D. *Gaussian Mixture Models*, 659–663 (Springer US, Boston, MA, 2009). URL https://doi.org/10.1007/978-0-387-73003-5_196.
- [56] Satija Lab. *panc8.SeuratData: Eight Pancreas Datasets Across Five Technologies* (2019). R package version 3.0.2.
- [57] Kang, H. M. *et al.* Multiplexed droplet single-cell rna-sequencing using natural genetic variation. *Nature Biotechnology* **36**, 89–94 (2018). URL <https://doi.org/10.1038/nbt.4042>.

E Supplement to “Assessing and improving reliability of neighbor embedding methods: a map-continuity perspective”

E.1 Derivation of singularity score

Given an input data matrix $\mathbf{X} = [\mathbf{x}_1, \dots, \mathbf{x}_n]^\top$ and its embedding matrix $\mathbf{Y} = [\mathbf{y}_1, \dots, \mathbf{y}_n]^\top$, without loss of generality, we will derive singularity score for the n -th embedding point. Singularity score measures the sensitivity of the embedding point under infinitesimal perturbation. Therefore, we add an infinitesimal perturbation of length ϵ and direction as a vector \mathbf{e} of unit length to \mathbf{x}_n to analyze the sensitivity of its embedding \mathbf{y}_n .

We note that \mathbf{y}_n is the minimizer of the partial LOO loss involving the n -th embedding point:

$$\mathbf{y}_n = \operatorname{argmin}_{\mathbf{y} \in \mathbb{R}^2} \sum_{1 \leq i \leq n-1} \mathcal{L}(w(\mathbf{y}_i, \mathbf{y}); v_{i,n}(\mathbf{X})) + Z([\mathbf{y}_1, \dots, \mathbf{y}_{n-1}, \mathbf{y}]^\top)$$

and denote the perturbed dataset as $\widetilde{\mathbf{X}}$ and $\tilde{\mathbf{y}}_n = \mathbf{f}_n(\mathbf{x}_n + \epsilon \mathbf{e})$, which is the mapping of perturbed \mathbf{x}_n by LOO-map, we have

$$\tilde{\mathbf{y}}_n = \operatorname{argmin}_{\mathbf{y} \in \mathbb{R}^2} \sum_{1 \leq i \leq n-1} \mathcal{L}(w(\mathbf{y}_i, \mathbf{y}); v_{i,n}(\widetilde{\mathbf{X}})) + Z([\mathbf{y}_1, \dots, \mathbf{y}_{n-1}, \mathbf{y}]^\top).$$

By first order condition, we have

$$\left[\sum_{1 \leq i \leq n-1} \left(\frac{\partial \mathcal{L}(w(\mathbf{y}_i, \mathbf{y}); v_{i,n}(\mathbf{X}))}{\partial \mathbf{y}} \right) + \frac{\partial Z([\mathbf{y}_1, \dots, \mathbf{y}_{n-1}, \mathbf{y}]^\top)}{\partial \mathbf{y}} \right] \Bigg|_{\mathbf{y}=\mathbf{y}_n} = \mathbf{0}, \quad (\text{S1})$$

$$\left[\sum_{1 \leq i \leq n-1} \left(\frac{\partial \mathcal{L}(w(\mathbf{y}_i, \mathbf{y}); v_{i,n}(\widetilde{\mathbf{X}}))}{\partial \mathbf{y}} \right) + \frac{\partial Z([\mathbf{y}_1, \dots, \mathbf{y}_{n-1}, \mathbf{y}]^\top)}{\partial \mathbf{y}} \right] \Bigg|_{\mathbf{y}=\tilde{\mathbf{y}}_n} = \mathbf{0}. \quad (\text{S2})$$

By doing Taylor’s expansion to $\frac{\partial \mathcal{L}(w(\mathbf{y}_i, \mathbf{y}); v_{i,n}(\widetilde{\mathbf{X}}))}{\partial \mathbf{y}} \Big|_{\mathbf{y}=\tilde{\mathbf{y}}_n}$ on $\tilde{\mathbf{y}}_n$ and $v_{i,n}(\widetilde{\mathbf{X}})$ for $i = 1, \dots, n-1$, we obtain

$$\begin{aligned} & \frac{\partial \mathcal{L}(w(\mathbf{y}_i, \mathbf{y}); v_{i,n}(\widetilde{\mathbf{X}}))}{\partial \mathbf{y}} \Bigg|_{\mathbf{y}=\tilde{\mathbf{y}}_n} \\ &= \frac{\partial \mathcal{L}(w(\mathbf{y}_i, \mathbf{y}); v_{i,n}(\mathbf{X}))}{\partial \mathbf{y}} \Bigg|_{\mathbf{y}=\mathbf{y}_n} + \frac{\partial^2 \mathcal{L}(w(\mathbf{y}_i, \mathbf{y}); v_{i,n}(\mathbf{X}))}{\partial \mathbf{y} \partial \mathbf{y}^\top} \Bigg|_{\mathbf{y}=\mathbf{y}_n} (\tilde{\mathbf{y}}_n - \mathbf{y}_n) \\ & \quad + \frac{\partial^2 \mathcal{L}(w(\mathbf{y}_i, \mathbf{y}); v)}{\partial \mathbf{y} \partial v} \Bigg|_{\mathbf{y}=\mathbf{y}_n, v=v_{i,n}(\mathbf{X})} (v_{i,n}(\widetilde{\mathbf{X}}) - v_{i,n}(\mathbf{X})) \\ & \quad + o(\|\tilde{\mathbf{y}}_n - \mathbf{y}_n\| + \|v_{i,n}(\widetilde{\mathbf{X}}) - v_{i,n}(\mathbf{X})\|). \end{aligned}$$

Then by doing Taylor’s expansion to $\frac{\partial Z([\mathbf{y}_1, \dots, \mathbf{y}_{n-1}, \mathbf{y}]^\top)}{\partial \mathbf{y}} \Big|_{\mathbf{y}=\tilde{\mathbf{y}}_n}$ on $\tilde{\mathbf{y}}_n$, we have

$$\begin{aligned} & \frac{\partial Z([\mathbf{y}_1, \dots, \mathbf{y}_{n-1}, \mathbf{y}]^\top)}{\partial \mathbf{y}} \Bigg|_{\mathbf{y}=\tilde{\mathbf{y}}_n} \\ &= \frac{\partial Z([\mathbf{y}_1, \dots, \mathbf{y}_{n-1}, \mathbf{y}]^\top)}{\partial \mathbf{y}} \Bigg|_{\mathbf{y}=\mathbf{y}_n} + \frac{\partial^2 Z([\mathbf{y}_1, \dots, \mathbf{y}_{n-1}, \mathbf{y}]^\top)}{\partial \mathbf{y} \partial \mathbf{y}^\top} \Bigg|_{\mathbf{y}=\mathbf{y}_n} (\tilde{\mathbf{y}}_n - \mathbf{y}_n) + o(\|\tilde{\mathbf{y}}_n - \mathbf{y}_n\|). \end{aligned}$$

Note that the embedding points and similarity scores are all functions of the input \mathbf{X} . We can do Taylor's expansion to both $\tilde{\mathbf{y}}_n$ and $v_{i,n}(\tilde{\mathbf{X}})$:

$$\begin{aligned}\tilde{\mathbf{y}}_n - \mathbf{y}_n &= \epsilon \left(\frac{\partial \mathbf{y}_n}{\partial \mathbf{x}_n} \right)^\top \mathbf{e} + o(\epsilon), \\ v_{i,n}(\tilde{\mathbf{X}}) - v_{i,n}(\mathbf{X}) &= \epsilon \left(\frac{\partial v_{i,n}(\mathbf{X})}{\partial \mathbf{x}_n} \right)^\top \mathbf{e} + o(\epsilon).\end{aligned}$$

Plug in, we have

$$\begin{aligned}& \left. \frac{\partial \mathcal{L}(w(\mathbf{y}_i, \mathbf{y}); v_{i,n}(\tilde{\mathbf{X}}))}{\partial \mathbf{y}} \right|_{\mathbf{y}=\tilde{\mathbf{y}}_n} \\ &= \left. \frac{\partial \mathcal{L}(w(\mathbf{y}_i, \mathbf{y}); v_{i,n}(\mathbf{X}))}{\partial \mathbf{y}} \right|_{\mathbf{y}=\mathbf{y}_n} + \epsilon \left. \frac{\partial^2 \mathcal{L}(w(\mathbf{y}_i, \mathbf{y}); v_{i,n}(\mathbf{X}))}{\partial \mathbf{y} \partial \mathbf{y}^\top} \right|_{\mathbf{y}=\mathbf{y}_n} \left(\frac{\partial \mathbf{y}_n}{\partial \mathbf{x}_n} \right)^\top \mathbf{e} \\ &+ \epsilon \left. \frac{\partial^2 \mathcal{L}(w(\mathbf{y}_i, \mathbf{y}); v)}{\partial \mathbf{y} \partial v} \right|_{\mathbf{y}=\mathbf{y}_n, v=v_{i,n}(\mathbf{X})} \left(\frac{\partial v_{i,n}(\mathbf{X})}{\partial \mathbf{x}_n} \right)^\top \mathbf{e} + o(\epsilon)\end{aligned} \quad (\text{S3})$$

and

$$\begin{aligned}& \left. \frac{\partial Z([\mathbf{y}_1, \dots, \mathbf{y}_{n-1}, \mathbf{y}]^\top)}{\partial \mathbf{y}} \right|_{\mathbf{y}=\tilde{\mathbf{y}}_n} \\ &= \left. \frac{\partial Z([\mathbf{y}_1, \dots, \mathbf{y}_{n-1}, \mathbf{y}]^\top)}{\partial \mathbf{y}} \right|_{\mathbf{y}=\mathbf{y}_n} + \epsilon \left. \frac{\partial Z([\mathbf{y}_1, \dots, \mathbf{y}_{n-1}, \mathbf{y}]^\top)}{\partial \mathbf{y} \partial \mathbf{y}^\top} \right|_{\mathbf{y}=\mathbf{y}_n} \left(\frac{\partial \mathbf{y}_n}{\partial \mathbf{x}_n} \right)^\top \mathbf{e} + o(\epsilon).\end{aligned} \quad (\text{S4})$$

By summing up Eqn. S3 for $i = 1, \dots, n-1$ and Eqn. S4, we have

$$\begin{aligned}& \left[\sum_{1 \leq i \leq n-1} \left(\frac{\partial \mathcal{L}(w(\mathbf{y}_i, \mathbf{y}); v_{i,n}(\tilde{\mathbf{X}}))}{\partial \mathbf{y}} \right) + \frac{\partial Z([\mathbf{y}_1, \dots, \mathbf{y}_{n-1}, \mathbf{y}]^\top)}{\partial \mathbf{y}} \right] \Bigg|_{\mathbf{y}=\tilde{\mathbf{y}}_n} \\ &= \left[\sum_{1 \leq i \leq n-1} \left(\frac{\partial \mathcal{L}(w(\mathbf{y}_i, \mathbf{y}); v_{i,n}(\mathbf{X}))}{\partial \mathbf{y}} \right) + \frac{\partial Z([\mathbf{y}_1, \dots, \mathbf{y}_{n-1}, \mathbf{y}]^\top)}{\partial \mathbf{y}} \right] \Bigg|_{\mathbf{y}=\mathbf{y}_n} \\ &+ \epsilon \frac{\partial^2 [\sum_{1 \leq i \leq n-1} \mathcal{L}(w(\mathbf{y}_i, \mathbf{y}); v_{i,n}(\mathbf{X})) + Z([\mathbf{y}_1, \dots, \mathbf{y}_{n-1}, \mathbf{y}]^\top)]}{\partial \mathbf{y} \partial \mathbf{y}^\top} \Bigg|_{\mathbf{y}=\mathbf{y}_n} \left(\frac{\partial \mathbf{y}_n}{\partial \mathbf{x}_n} \right)^\top \mathbf{e} \\ &+ \epsilon \sum_{1 \leq i \leq n-1} \left[\left. \frac{\partial^2 \mathcal{L}(w(\mathbf{y}_i, \mathbf{y}); v)}{\partial \mathbf{y} \partial v} \right|_{\mathbf{y}=\mathbf{y}_n, v=v_{i,n}(\mathbf{X})} \left(\frac{\partial v_{i,n}(\mathbf{X})}{\partial \mathbf{x}_n} \right)^\top \right] \mathbf{e} + o(\epsilon).\end{aligned}$$

Also note that

$$\frac{\partial^2 [\sum_{1 \leq i \leq n-1} \mathcal{L}(w(\mathbf{y}_i, \mathbf{y}); v_{i,n}(\mathbf{X})) + Z([\mathbf{y}_1, \dots, \mathbf{y}_{n-1}, \mathbf{y}]^\top)]}{\partial \mathbf{y} \partial \mathbf{y}^\top} = \frac{\partial^2 \mathfrak{L}(\mathbf{y}_1, \dots, \mathbf{y}_{n-1}, \mathbf{y}; \mathbf{X})}{\partial \mathbf{y} \partial \mathbf{y}^\top}$$

where \mathfrak{L} denotes the total loss:

$$\mathfrak{L}(\mathbf{y}_1, \dots, \mathbf{y}_n; \mathbf{X}) = \sum_{1 \leq i < j \leq n} \mathcal{L}(w(\mathbf{y}_i, \mathbf{y}_j); v_{i,j}(\mathbf{X})) + Z([\mathbf{y}_1, \dots, \mathbf{y}_n]^\top).$$

Plug in the first order condition Eqn. S1 and Eqn. S2, we have the change of \mathbf{y}_n after the infinitesimal perturbation as

$$\begin{aligned}\tilde{\mathbf{y}}_n - \mathbf{y}_n &= \epsilon \left(\frac{\partial \mathbf{y}_n}{\partial \mathbf{x}_n} \right)^\top \mathbf{e} + o(\epsilon) \\ &= -\epsilon \mathbf{H}_n^{-1} \sum_{1 \leq i \leq n-1} \left[\left. \frac{\partial^2 \mathcal{L}(w(\mathbf{y}_i, \mathbf{y}); v)}{\partial \mathbf{y} \partial v} \right|_{\mathbf{y}=\mathbf{y}_n, v=v_{i,n}(\mathbf{X})} \left(\frac{\partial v_{i,n}(\mathbf{X})}{\partial \mathbf{x}_n} \right)^\top \right] \mathbf{e} + o(\epsilon)\end{aligned}$$

where \mathbf{H}_n denote the Hessian matrix of the loss function with respect to \mathbf{y}_n :

$$\mathbf{H}_n = \frac{\partial^2 \mathcal{L}(\mathbf{y}_1, \dots, \mathbf{y}_{n-1}, \mathbf{y}; \mathbf{X})}{\partial \mathbf{y} \partial \mathbf{y}^\top} \Big|_{\mathbf{y}=\mathbf{y}_n}.$$

Importantly, \mathbf{H}_n is independent of the perturbation direction e . A singular Hessian matrix results in the most extreme local discontinuity. The more singular \mathbf{H}_n is, the more sensitive the embedding of \mathbf{x}_n becomes to infinitesimal perturbations. This is why we define the singularity score for the n -th data point as $\lambda_{\min}^{-1}(\mathbf{H}_n)$. The higher the singularity score, the more singular \mathbf{H}_n is, and the greater the sensitivity of the embedding of \mathbf{x}_n to infinitesimal perturbations.

E.2 Singularity scores for t-SNE, UMAP, LargeVis

We have the detailed singularity scores for t-SNE, UMAP, LargeVis as follows.

Singularity score for t-SNE. The total loss for t-SNE is

$$\begin{aligned} \mathcal{L}(\mathbf{y}_1, \dots, \mathbf{y}_n; \mathbf{X}) &= \sum_{1 \leq i < j \leq n} \mathcal{L}(w(\mathbf{y}_i, \mathbf{y}_j); v_{i,j}(\mathbf{X})) + Z([\mathbf{y}_1, \dots, \mathbf{y}_n]^\top), \quad \text{where} \\ \mathcal{L}(w(\mathbf{y}_i, \mathbf{y}_j); v_{i,j}(\mathbf{X})) &= -2v_{i,j}(\mathbf{X}) \log(w(\mathbf{y}_i, \mathbf{y}_j)), \quad w(\mathbf{y}_i, \mathbf{y}_j) = (1 + \|\mathbf{y}_i - \mathbf{y}_j\|_2^2)^{-1}, \\ Z([\mathbf{y}_1, \dots, \mathbf{y}_n]^\top) &= \log \left(\sum_{k,l:k \neq l} (1 + \|\mathbf{y}_k - \mathbf{y}_l\|_2^2)^{-1} \right). \end{aligned}$$

Then, the singularity score for the i -th t-SNE embedding point is $\lambda_{\min}^{-1}(\mathbf{H}_i)$, where

$$\begin{aligned} \mathbf{H}_i &= \frac{\partial \mathcal{L}}{\partial \mathbf{y}_i \partial \mathbf{y}_i^\top} = - \sum_{j:j \neq i} \mathbf{H}_{ij}, \quad \text{where} \\ \mathbf{H}_{ij} &= \frac{\partial \mathcal{L}}{\partial \mathbf{y}_i \partial \mathbf{y}_j^\top} = -4v_{i,j}(\mathbf{X})w(\mathbf{y}_i, \mathbf{y}_j)\mathbf{I}_2 + 8v_{i,j}(\mathbf{X})w^2(\mathbf{y}_i, \mathbf{y}_j)(\mathbf{y}_i - \mathbf{y}_j)(\mathbf{y}_i - \mathbf{y}_j)^\top \\ &\quad - 16 \left(\sum_{k,l:k \neq l} w(\mathbf{y}_k, \mathbf{y}_l) \right)^{-2} \left(\sum_{l:l \neq j} (w^2(\mathbf{y}_j, \mathbf{y}_l)(\mathbf{y}_j - \mathbf{y}_l)) \right) \left(\sum_{l:l \neq i} (w^2(\mathbf{y}_i, \mathbf{y}_l)(\mathbf{y}_i - \mathbf{y}_l)) \right)^\top \\ &\quad + 4 \left(\sum_{k,l:k \neq l} w(\mathbf{y}_k, \mathbf{y}_l) \right)^{-1} w^2(\mathbf{y}_i, \mathbf{y}_j)\mathbf{I}_2 - 16 \left(\sum_{k,l:k \neq l} w(\mathbf{y}_k, \mathbf{y}_l) \right)^{-1} w^3(\mathbf{y}_i, \mathbf{y}_j)(\mathbf{y}_i - \mathbf{y}_j)(\mathbf{y}_i - \mathbf{y}_j)^\top. \end{aligned}$$

Singularity score for UMAP. The total loss for UMAP is

$$\begin{aligned} \mathcal{L}(\mathbf{y}_1, \dots, \mathbf{y}_n; \mathbf{X}) &= \sum_{1 \leq i < j \leq n} \mathcal{L}(w(\mathbf{y}_i, \mathbf{y}_j); v_{i,j}(\mathbf{X})) + Z([\mathbf{y}_1, \dots, \mathbf{y}_n]^\top), \quad \text{where} \\ \mathcal{L}(w(\mathbf{y}_i, \mathbf{y}_j); v_{i,j}(\mathbf{X})) &= -v_{i,j}(\mathbf{X}) \log(w(\mathbf{y}_i, \mathbf{y}_j)) - (1 - v_{i,j}(\mathbf{X})) \log(1 - w(\mathbf{y}_i, \mathbf{y}_j)), \\ w(\mathbf{y}_i, \mathbf{y}_j) &= (1 + a\|\mathbf{y}_i - \mathbf{y}_j\|_2^{2b})^{-1}, \quad Z([\mathbf{y}_1, \dots, \mathbf{y}_n]^\top) = 0, \end{aligned}$$

in which a and b are the hyperparameters chosen by user.

Then, the singularity score for the i -th UMAP embedding point is $\lambda_{\min}^{-1}(\mathbf{H}_i)$, where

$$\begin{aligned}
\mathbf{H}_i &= \sum_{k:k \neq i} 2abv_{i,k}(\mathbf{X})w(\mathbf{y}_i, \mathbf{y}_k)\|\mathbf{y}_i - \mathbf{y}_k\|_2^{2(b-1)}\mathbf{I}_2 \\
&\quad - \sum_{k:k \neq i} 4a^2b^2v_{i,k}(\mathbf{X})w^2(\mathbf{y}_i, \mathbf{y}_k)\|\mathbf{y}_i - \mathbf{y}_k\|_2^{4(b-1)}(\mathbf{y}_i - \mathbf{y}_k)(\mathbf{y}_i - \mathbf{y}_k)^\top \\
&\quad + \sum_{k:k \neq i} 4ab(b-1)v_{i,k}(\mathbf{X})w(\mathbf{y}_i, \mathbf{y}_k)\|\mathbf{y}_i - \mathbf{y}_k\|_2^{2(b-2)}(\mathbf{y}_i - \mathbf{y}_k)(\mathbf{y}_i - \mathbf{y}_k)^\top \\
&\quad - \sum_{k:k \neq i} 2ab(1-v_{i,k}(\mathbf{X}))w^2(\mathbf{y}_i, \mathbf{y}_k)(1-w(\mathbf{y}_i, \mathbf{y}_k))^{-1}\|\mathbf{y}_i - \mathbf{y}_k\|_2^{2(b-1)}\mathbf{I}_2 \\
&\quad + \sum_{k:k \neq i} \frac{a^2b^2w^4(\mathbf{y}_i, \mathbf{y}_k)(8w^{-1}(\mathbf{y}_i, \mathbf{y}_k) - 4)}{(1-w(\mathbf{y}_i, \mathbf{y}_k))^2}(1-v_{i,k}(\mathbf{X}))\|\mathbf{y}_i - \mathbf{y}_k\|_2^{4(b-1)}(\mathbf{y}_i - \mathbf{y}_k)(\mathbf{y}_i - \mathbf{y}_k)^\top \\
&\quad - \sum_{k:k \neq i} \frac{4ab(b-1)w^2(\mathbf{y}_i, \mathbf{y}_k)}{1-w(\mathbf{y}_i, \mathbf{y}_k)}(1-v_{i,k}(\mathbf{X}))\|\mathbf{y}_i - \mathbf{y}_k\|_2^{2(b-2)}(\mathbf{y}_i - \mathbf{y}_k)(\mathbf{y}_i - \mathbf{y}_k)^\top.
\end{aligned}$$

Singularity score for LargeVis. The total loss for LargeVis is

$$\begin{aligned}
\mathcal{L}(\mathbf{y}_1, \dots, \mathbf{y}_n; \mathbf{X}) &= \sum_{1 \leq i < j \leq n} \mathcal{L}(w(\mathbf{y}_i, \mathbf{y}_j); v_{i,j}(\mathbf{X})) + Z([\mathbf{y}_1, \dots, \mathbf{y}_n]^\top), \quad \text{where} \\
\mathcal{L}(w(\mathbf{y}_i, \mathbf{y}_j); v_{i,j}(\mathbf{X})) &= \mathbb{1}_{\{(i,j) \in E\}} v_{i,j}(\mathbf{X}) \log(w(\mathbf{y}_i, \mathbf{y}_j)) + \gamma \mathbb{1}_{\{(i,j) \notin E\}} \log(1-w(\mathbf{y}_i, \mathbf{y}_j)), \\
w(\mathbf{y}_i, \mathbf{y}_j) &= f(\|\mathbf{y}_i - \mathbf{y}_j\|_2), \quad f(x) = (1+x^2)^{-1}, \quad Z([\mathbf{y}_1, \dots, \mathbf{y}_n]^\top) = 0,
\end{aligned}$$

in which E is the set of edges in the pre-constructed neighbor graph and γ is an unified weight assigned to the negative edges.

Then, the singularity score for the i -th LargeVis embedding point is $\lambda_{\min}^{-1}(\mathbf{H}_i)$, where

$$\begin{aligned}
\mathbf{H}_i &= - \sum_{k:k \neq i} (\mathbb{1}_{\{(i,k) \in E\}} v_{i,k}(\mathbf{X}) + \gamma \mathbb{1}_{\{(i,k) \notin E\}}) (2w(\mathbf{y}_i, \mathbf{y}_k)\mathbf{I}_2 - 4w^2(\mathbf{y}_i, \mathbf{y}_k)(\mathbf{y}_i - \mathbf{y}_k)(\mathbf{y}_i - \mathbf{y}_k)^\top) \\
&\quad + \sum_{k:k \neq i} \gamma \mathbb{1}_{\{(i,k) \notin E\}} \left(\frac{2\mathbf{I}_2}{\|\mathbf{y}_i - \mathbf{y}_k\|_2^2} - \frac{4(\mathbf{y}_i - \mathbf{y}_k)(\mathbf{y}_i - \mathbf{y}_k)^\top}{\|\mathbf{y}_i - \mathbf{y}_k\|_2^4} \right).
\end{aligned}$$

E.3 Proof of Theoretical Result

E.3.1 Interpolation Property of the LOO-map

Proposition 1. Given $\mathbf{X} = [\mathbf{x}_1, \dots, \mathbf{x}_n]^\top$ and their corresponding embedding points $\mathbf{Y} = [\mathbf{y}_1, \dots, \mathbf{y}_n]^\top$, under the LOO assumption, the LOO-map \mathbf{f} induced by \mathbf{X} and \mathbf{Y} exhibits the interpolation property such that

$$\mathbf{f}(\mathbf{x}_i) \approx \mathbf{y}_i, \quad i = 1, \dots, n.$$

The proof of Proposition 1 is as follows.

Without loss of generality, we will prove $\mathbf{f}(\mathbf{x}_n) \approx \mathbf{y}_n$. For a dataset $\widetilde{\mathbf{X}} = [\mathbf{x}_1, \dots, \mathbf{x}_n, \mathbf{x}_{n+1}]^\top$ where $\mathbf{x}_{n+1} = \mathbf{x}_n$ and their embedding points $[\tilde{\mathbf{y}}_1, \dots, \tilde{\mathbf{y}}_n, \tilde{\mathbf{y}}_{n+1}]^\top$, note that the similarity scores are equal for \mathbf{x}_n and \mathbf{x}_{n+1} , i.e., $v_{i,n}(\widetilde{\mathbf{X}}) = v_{i,n+1}(\widetilde{\mathbf{X}}), \forall i$. Thus,

$$\frac{\partial \mathcal{L}(\tilde{\mathbf{y}}_1, \dots, \tilde{\mathbf{y}}_n, \tilde{\mathbf{y}}_{n+1}; \widetilde{\mathbf{X}})}{\partial \tilde{\mathbf{y}}_n} = \frac{\partial \mathcal{L}(\tilde{\mathbf{y}}_1, \dots, \tilde{\mathbf{y}}_n, \tilde{\mathbf{y}}_{n+1}; \widetilde{\mathbf{X}})}{\partial \tilde{\mathbf{y}}_{n+1}}.$$

Using standard gradient descent and momentum methods, as employed in the t-SNE algorithm, with equal initializations for \mathbf{y}_n and \mathbf{y}_{n+1} (e.g., PCA initialization), we observe that for any iteration step t , $\tilde{\mathbf{y}}_n^{(t)} = \tilde{\mathbf{y}}_{n+1}^{(t)}$. In this way, a local minima of \mathcal{L} , i.e., the embedding of $\tilde{\mathbf{X}}$ can be obtained with $\tilde{\mathbf{y}}_n = \tilde{\mathbf{y}}_{n+1}$.

The LOO-map is defined as

$$\begin{aligned} \mathbf{f}(\mathbf{x}) &= \operatorname{argmin}_{\mathbf{y}} L(\mathbf{y}; \mathbf{x}), \quad \text{where} \\ L(\mathbf{y}; \mathbf{x}) &= \sum_{1 \leq i \leq n} \mathcal{L}\left(w(\mathbf{y}_i, \mathbf{y}); v_{i,n+1}\left(\begin{bmatrix} \mathbf{X} \\ \mathbf{x} \end{bmatrix}\right)\right) + Z\left(\begin{bmatrix} \mathbf{Y} \\ \mathbf{y} \end{bmatrix}\right). \end{aligned}$$

The LOO assumption yields that $\mathbf{y}_i \approx \tilde{\mathbf{y}}_i$ for $i = 1, \dots, n$. Therefore, we have

$$L(\mathbf{y}; \mathbf{x}) \approx L_{n+1}(\mathbf{y}; \mathbf{x}) = \sum_{1 \leq i \leq n} \mathcal{L}\left(w(\tilde{\mathbf{y}}_i, \mathbf{y}); v_{i,n+1}\left(\begin{bmatrix} \mathbf{X} \\ \mathbf{x} \end{bmatrix}\right)\right) + Z\left(\begin{bmatrix} \tilde{\mathbf{Y}} \\ \mathbf{y} \end{bmatrix}\right),$$

where $\tilde{\mathbf{Y}} = [\tilde{\mathbf{y}}_1, \dots, \tilde{\mathbf{y}}_n]^\top$. Note that $\tilde{\mathbf{y}}_n = \tilde{\mathbf{y}}_{n+1} = \operatorname{argmin}_{\mathbf{y}} L_{n+1}(\mathbf{y}; \mathbf{x}) \approx \operatorname{argmin}_{\mathbf{y}} L(\mathbf{y}; \mathbf{x})$. Therefore, we have

$$\mathbf{f}(\mathbf{x}_n) \approx \tilde{\mathbf{y}}_n.$$

E.3.2 Hyperbolic Structure in the LOO Loss: Proof of Theorem 1

In this subsection, we will prove Theorem 1. From basic calculation, we have

$$\begin{aligned} -\nabla_{\mathbf{y}} L(\mathbf{y}; \mathbf{x}^\varepsilon) &= \mathbf{F}_a + \mathbf{F}_r, \quad \text{where} \\ \mathbf{F}_a &= 4 \sum_{i=1}^n \frac{v_{i,n+1}}{1 + \|\mathbf{y}_i - \mathbf{y}\|^2} (\mathbf{y}_i - \mathbf{y}), \\ \mathbf{F}_r &= -\frac{4}{Z} \sum_{i=1}^n \frac{1}{(1 + \|\mathbf{y}_i - \mathbf{y}\|^2)^2} (\mathbf{y}_i - \mathbf{y}) \end{aligned}$$

Let us simplify \mathbf{F}_a and \mathbf{F}_r using the asymptotics we assumed in the theorem. First we observe that

$$\begin{aligned} \frac{1}{1 + \|\pm \boldsymbol{\theta} - \mathbf{y} + \boldsymbol{\delta}_i\|^2} &= \frac{1}{1 + \|\boldsymbol{\theta}\|^2 + 2\langle \pm \boldsymbol{\theta}, -\mathbf{y} + \boldsymbol{\delta}_i \rangle + \|\mathbf{y} - \boldsymbol{\delta}_i\|^2} \\ &= \frac{1}{\|\boldsymbol{\theta}\|^2} \left[1 - 2 \left\langle \pm \frac{\boldsymbol{\theta}}{\|\boldsymbol{\theta}\|^2}, -\mathbf{y} + \boldsymbol{\delta}_i \right\rangle + O\left(\frac{1}{\|\boldsymbol{\theta}\|^2}\right) \right] \end{aligned}$$

If $i \in \mathcal{I}_+$, then

$$\begin{aligned} \frac{\mathbf{y}_i - \mathbf{y}}{1 + \|\boldsymbol{\theta} - \mathbf{y} + \boldsymbol{\delta}_i\|^2} &= \frac{\boldsymbol{\theta} + \boldsymbol{\delta}_i - \mathbf{y}}{\|\boldsymbol{\theta}\|^2} \left[1 - 2 \left\langle \frac{\boldsymbol{\theta}}{\|\boldsymbol{\theta}\|^2}, -\mathbf{y} + \boldsymbol{\delta}_i \right\rangle + O\left(\frac{1}{\|\boldsymbol{\theta}\|^2}\right) \right] \\ &= \frac{\boldsymbol{\theta}}{\|\boldsymbol{\theta}\|^2} + \frac{\boldsymbol{\delta}_i - \mathbf{y}}{\|\boldsymbol{\theta}\|^2} - \frac{2\boldsymbol{\theta}}{\|\boldsymbol{\theta}\|^2} \left\langle \frac{\boldsymbol{\theta}}{\|\boldsymbol{\theta}\|^2}, -\mathbf{y} + \boldsymbol{\delta}_i \right\rangle + O\left(\frac{1}{\|\boldsymbol{\theta}\|^3}\right); \end{aligned}$$

if $i \in \mathcal{I}_-$, then

$$\begin{aligned} \frac{\mathbf{y}_i - \mathbf{y}}{1 + \|\mathbf{y} - \boldsymbol{\theta} + \boldsymbol{\delta}_i\|^2} &= \frac{-\boldsymbol{\theta} + \boldsymbol{\delta}_i - \mathbf{y}}{\|\boldsymbol{\theta}\|^2} \left[1 - 2 \left\langle -\frac{\boldsymbol{\theta}}{\|\boldsymbol{\theta}\|^2}, -\mathbf{y} + \boldsymbol{\delta}_i \right\rangle + O\left(\frac{1}{\|\boldsymbol{\theta}\|^2}\right) \right] \\ &= -\frac{\boldsymbol{\theta}}{\|\boldsymbol{\theta}\|^2} + \frac{\boldsymbol{\delta}_i - \mathbf{y}}{\|\boldsymbol{\theta}\|^2} - \frac{2\boldsymbol{\theta}}{\|\boldsymbol{\theta}\|^2} \left\langle \frac{\boldsymbol{\theta}}{\|\boldsymbol{\theta}\|^2}, -\mathbf{y} + \boldsymbol{\delta}_i \right\rangle + O\left(\frac{1}{\|\boldsymbol{\theta}\|^3}\right). \end{aligned}$$

Since $\sum_i \delta_i = \mathbf{0}$, we have

$$\frac{1}{n} \sum_{i=1}^n \frac{\mathbf{y}_i - \mathbf{y}}{1 + \|\mathbf{y}_i - \mathbf{y}\|^2} = -\frac{\mathbf{y}}{\|\boldsymbol{\theta}\|^2} + \frac{2}{\|\boldsymbol{\theta}\|^2} \mathbf{y}_{//} + O\left(\frac{1}{\|\boldsymbol{\theta}\|^3}\right).$$

Similarly,

$$\frac{1}{n} \sum_{i \in \mathcal{I}_+} \frac{\mathbf{y}_i - \mathbf{y}}{1 + \|\mathbf{y}_i - \mathbf{y}\|^2} - \frac{1}{n} \sum_{i \in \mathcal{I}_-} \frac{\mathbf{y}_i - \mathbf{y}}{1 + \|\mathbf{y}_i - \mathbf{y}\|^2} = \frac{2\boldsymbol{\theta}}{\|\boldsymbol{\theta}\|^2} + O\left(\frac{1}{\|\boldsymbol{\theta}\|^3}\right).$$

Therefore,

$$\mathbf{F}_a = \frac{4np_0(2\mathbf{y}_{//} - \mathbf{y})}{\|\boldsymbol{\theta}\|^2} + \frac{8n\epsilon\boldsymbol{\theta}}{\|\boldsymbol{\theta}\|^2} + O\left(\frac{1}{\|\boldsymbol{\theta}\|^3}\right). \quad (\text{S5})$$

To handle \mathbf{F}_r , we notice that

$$\frac{\mathbf{y}_i - \mathbf{y}}{(1 + \|\mathbf{y}_i - \mathbf{y}\|^2)^2} = O\left(\frac{1}{\|\boldsymbol{\theta}\|^3}\right).$$

Moreover,

$$\frac{1}{1 + \|\mathbf{y}_i - \mathbf{y}_j\|^2} \leq 1, \quad \implies \quad Z \leq n(n+1).$$

and also

$$Z \geq \sum_{i,j \in \mathcal{I}_+} \frac{1}{1 + \|\mathbf{y}_i - \mathbf{y}_j\|^2} = \sum_{i,j \in \mathcal{I}_+} \frac{1}{1 + \|\boldsymbol{\delta}_i - \boldsymbol{\delta}_j\|^2},$$

Thus, Z^{-1} is of constant order, so

$$\mathbf{F}_r = O\left(\frac{1}{\|\boldsymbol{\theta}\|^3}\right). \quad (\text{S6})$$

Combining Eqn. S5 and S6, we reach our conclusion.

E.4 Supplementary Tables and Figures

Dataset	Points	Dimensions	Domain	Usage
CIFAR-10 [49]	10,000	512	Deep learning	Perturbation score, verification of LOO assumption
DTD [50]	5,640	512	Deep learning	Perturbation score (OOD detection)
Embryo [51]	421	2,000	Single-cell	Singularity score
Brain [52]	3,618	1,000	Single-cell	Singularity score, verification of LOO assumption
IFNB [57]	6,548	2,000	Single-cell	Verification of LOO assumption
Panc8 [56]	2,364	2,000	Single-cell	Verification of LOO assumption

Table S1: **Datasets analyzed in this work.** This paper analyzes six real-world datasets: CIFAR-10, Describable Textures Dataset (DTD), the mouse embryonic stem cell differentiation data (Embryo), the single-cell RNA-seq dataset generated from PBMCs treated with interferon- β (IFNB), the mouse brain single-cell ATAC-seq data (Brain), the single-cell RNA-seq dataset generated from human pancreatic tissues (Panc8). The table lists the number of points, dimensions, domains, and usage of the datasets.

Dataset	Number of points	Perplexity 5	Perplexity 25	Perplexity 50	Perplexity 75
2-GMM	$n = 1000$	0.080 (0.0017)	0.068 (0.0035)	0.054 (0.0056)	0.048 (0.0124)
	$n = 3000$	0.071 (0.0008)	0.044 (0.0018)	0.036 (0.0022)	0.032 (0.0010)
	$n = 5000$	0.062 (0.0006)	0.034 (0.0007)	0.033 (0.0019)	0.032 (0.0017)
Swissroll	$n = 1000$	0.081 (0.0019)	0.074 (0.0110)	0.003 (0.0018)	0.002 (0.0005)
	$n = 3000$	0.072 (0.0006)	0.043 (0.0041)	0.0047 (0.0062)	0.038 (0.0068)
	$n = 5000$	0.063 (0.0007)	0.033 (0.0014)	0.031 (0.0034)	0.037 (0.0061)
Brain	$n = 1000$	0.082 (0.0032)	0.021 (0.0046)	0.005 (0.0030)	0.004 (0.0026)
	$n = 2000$	0.069 (0.0041)	0.038 (0.0042)	0.005 (0.0019)	0.003 (0.0012)
	$n = 3000$	0.063 (0.0016)	0.041 (0.0027)	0.016 (0.0030)	0.003 (0.0012)
Panc8	$n = 500$	0.094 (0.0024)	0.046 (0.0099)	0.030 (0.0357)	0.025 (0.0273)
	$n = 1200$	0.083 (0.0012)	0.064 (0.0016)	0.045 (0.0037)	0.028 (0.0066)
	$n = 2000$	0.079 (0.0013)	0.060 (0.0013)	0.049 (0.0028)	0.039 (0.0017)
IFNB	$n = 1000$	0.085 (0.0036)	0.069 (0.0022)	0.059 (0.0052)	0.052 (0.0107)
	$n = 3000$	0.064 (0.0015)	0.049 (0.0019)	0.048 (0.0033)	0.046 (0.0029)
	$n = 5000$	0.059 (0.0010)	0.044 (0.0010)	0.043 (0.0022)	0.040 (0.0015)
CIFAR10	$n = 1000$	0.086 (0.0019)	0.042 (0.0081)	0.017 (0.0231)	0.006 (0.0066)
	$n = 3000$	0.072 (0.0009)	0.044 (0.0013)	0.029 (0.0037)	0.023 (0.0113)
	$n = 5000$	0.065 (0.0004)	0.039 (0.0006)	0.029 (0.0009)	0.025 (0.0031)

Table S2: **Averaged (and std of) ϵ_n across multiple trials under different datasets and perplexities.** We measure the approximation error ϵ_n across 20 independent trials and report the mean (and standard error) of ϵ_n for each setting. We observe from the table that all ϵ_n 's are small and noticeably, ϵ_n is generally decreasing in n , which supports the LOO assumption.

Data	Perplexity	DB Index	WCDR	Wilks' Λ
2-GMM 2d	Perplexity 5	0.7470 (0.0401)	0.3625 (0.0242)	0.2244 (0.0170)
	Perplexity 50	0.3821 (0.0653)	0.1287 (0.0353)	0.0960 (0.0234)
2-GMM 10d	Perplexity 5	0.4580 (0.0082)	0.1760 (0.0050)	0.0803 (0.0066)
	Perplexity 50	0.1232 (0.0034)	0.0152 (0.0008)	0.0077 (0.0006)
2-GMM 50d	Perplexity 5	0.3943 (0.0090)	0.1372 (0.0053)	0.0697 (0.0045)
	Perplexity 45	0.1046 (0.0058)	0.0110 (0.0011)	0.0056 (0.0006)
5-GMM 2d	Perplexity 5	0.5226 (0.0286)	0.0776 (0.0067)	0.0061 (0.0012)
	Perplexity 65	0.2211 (0.0230)	0.0076 (0.0002)	6.00×10^{-6} (2.26×10^{-6})
5-GMM 10d	Perplexity 5	0.3550 (0.0228)	0.0331 (0.0025)	0.0014 (0.0003)
	Perplexity 40	0.2549 (0.0225)	0.0060 (0.0016)	0.0001 (6.16×10^{-5})
5-GMM 50d	Perplexity 5	0.2813 (0.0066)	0.0244 (0.0008)	0.0006 (0.0001)
	Perplexity 35	0.1627 (0.00091)	0.0048 (0.0005)	3.02×10^{-5} (4.85×10^{-6})

Table S3: **Clustering quality improves after selecting a perplexity based on singularity scores.** Across the various data distributions and dimensions listed in the table, increasing the perplexity up to the elbow point leads to a decrease in all three quantitative metrics, indicating an improvement in clustering quality.

	Class	Perplexity 4		Perplexity 25	
		<i>p</i> -value	Corrected <i>p</i> -value*	<i>p</i> -value	Corrected <i>p</i> -value*
Test for Spearman's Rank Correlation	1	0.0757	0.3026	0.0000	0.0000
	2	0.1298	0.3895	6.3×10^{-5}	1.9×10^{-4}
	3	0.0389	0.1945	2.7×10^{-5}	1.1×10^{-4}
	4	0.2493	0.4533	0.7408	0.7408
	5	0.2266	0.4533	4.0×10^{-3}	8.0×10^{-3}
F-test for Local Regression Model	<i>p</i> -value	0.2490		6.243×10^{-15}	
Permutation Test for Local Regression Model	<i>p</i> -value	0.1702		0.0000	

* Use Holm-Bonferroni correction for multiple testing.

(a) Tests of singularity score pattern in single-cell RNA-seq data of mouse embryonic stem cells (mESCs) differentiation.

	Class	Perplexity 5		Perplexity 95	
		<i>p</i> -value	Corrected <i>p</i> -value*	<i>p</i> -value	Corrected <i>p</i> -value*
Test for Spearman's Rank Correlation	Astrocytes	0.2136	1.0000	0.5048	0.5048
	Endothelial Cells	0.5594	1.0000	0.0651	0.1893
	Excitatory Neurons	0.7461	1.0000	1.2×10^{-5}	5.9×10^{-5}
	Inhibitory Neurons	0.0470	0.2820	0.0631	0.1893
	Microglia	0.3735	1.0000	1.2×10^{-7}	7.3×10^{-7}
	Oligodendrocytes	0.6364	1.0000	3.9×10^{-3}	0.0156
F-test for Local Regression Model	<i>p</i> -value	0.0868		$< 2.2 \times 10^{-16}$	
Permutation Test for Local Regression Model	<i>p</i> -value	0.0890		0.0000	

* Use Holm-Bonferroni correction for multiple testing.

(b) Tests of singularity score pattern in mouse brain single-cell ATAC-seq data.

Table S4: Tests of the distribution difference of singularity scores in (a) mouse embryonic stem cell differentiation data and (b) mouse brain chromatin accessibility data. We verify the distribution difference using Spearman's rank correlation tests between singularity scores and distances to cluster centers, F-tests and permutation tests for a local regression model (singularity scores regressed against locations). The results of all three tests confirm the distribution difference of singularity scores between small and large perplexities.

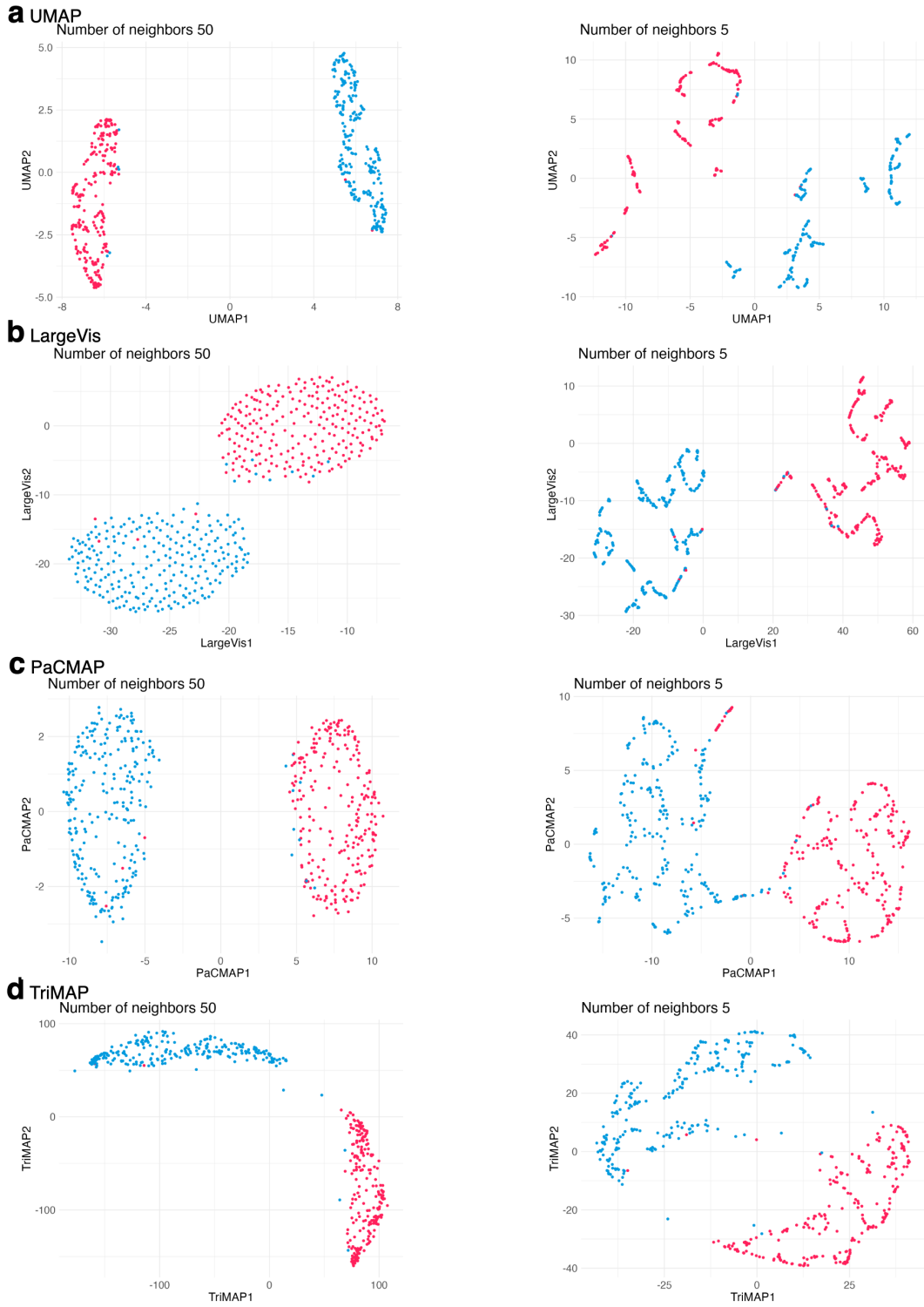


Figure S1: **OI and FI discontinuities are common among neighbor embedding methods.** We use the same setting as in Figure 3a, where we generate two-component Gaussian mixture data and embed the input points using various neighbor embedding methods, including UMAP (a), LargeVis (b), PaCMAP (c), TriMAP (d). The hyperparameter is the number of neighbors (similar to perplexity) chosen as 50 (left panels) and 5 (right panels) respectively. We observe similar OI and FI discontinuity as in the t-SNE method.

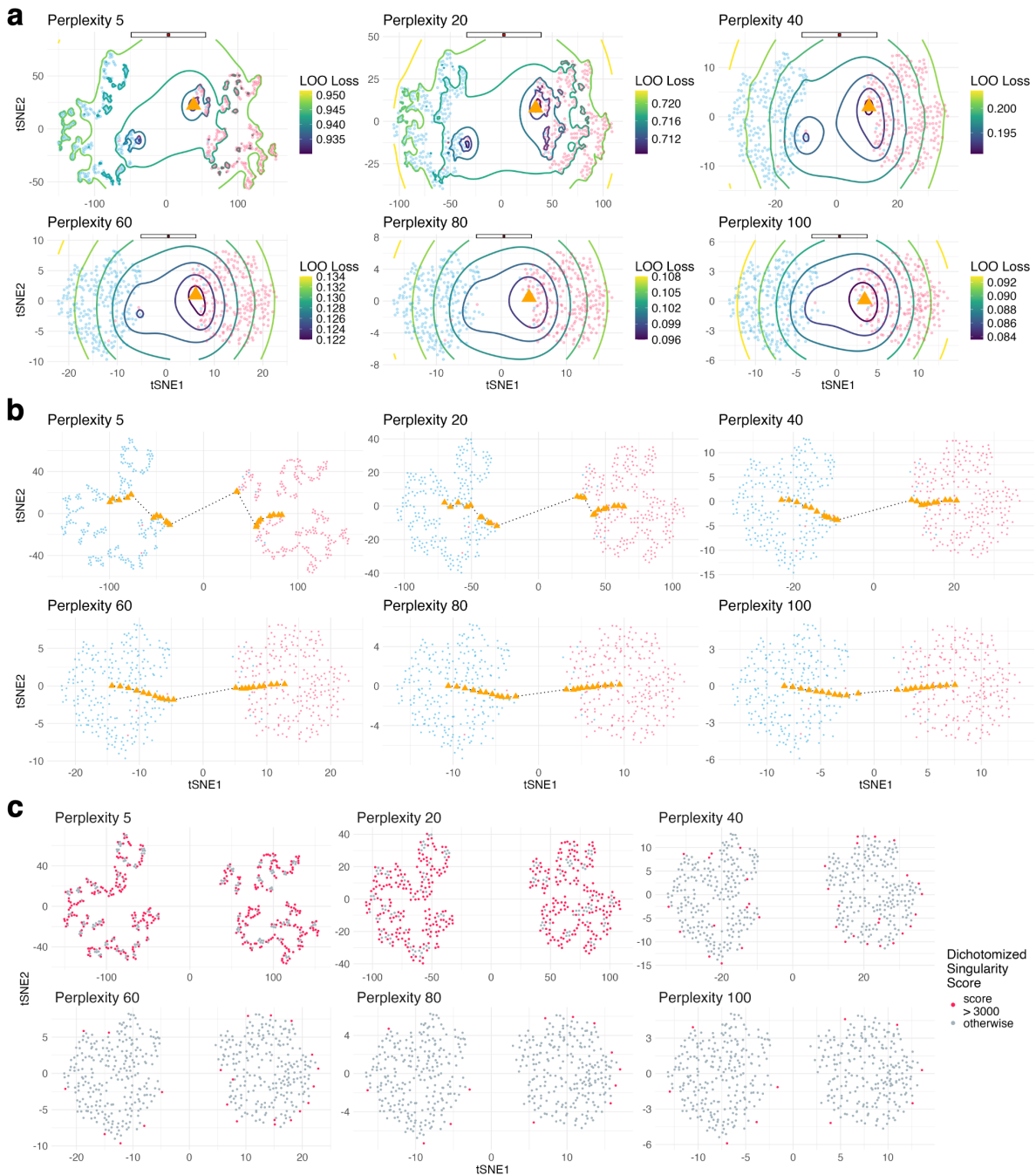


Figure S2: Large perplexity lessens FI discontinuity. We use the same mixture data as in Figure 3 and run the standard t-SNE algorithm 6 times at perplexity 5, 20, 40, 60, 80, 100. **a** Contour plot shows the landscape of LOO loss $L(y; x)$ for $x = 0.5(c_1 + c_2)$ under different perplexities. The number of local minima in the loss decreases with higher perplexity, indicating that the FI discontinuity lessens under higher perplexity. **b** Trajectories of the embedding point of x are shown with different perplexities. Under small perplexities, numerous local minima cause an uneven trajectory of embedding points when we add x at evenly interpolated locations; while under larger perplexities, the trajectory is more smooth. This further suggests a reduction of FI discontinuity when the perplexity increases. **c** Embeddings with dichotomized singularity scores. Embedding points with high singularity scores decrease in number when increasing the perplexity.

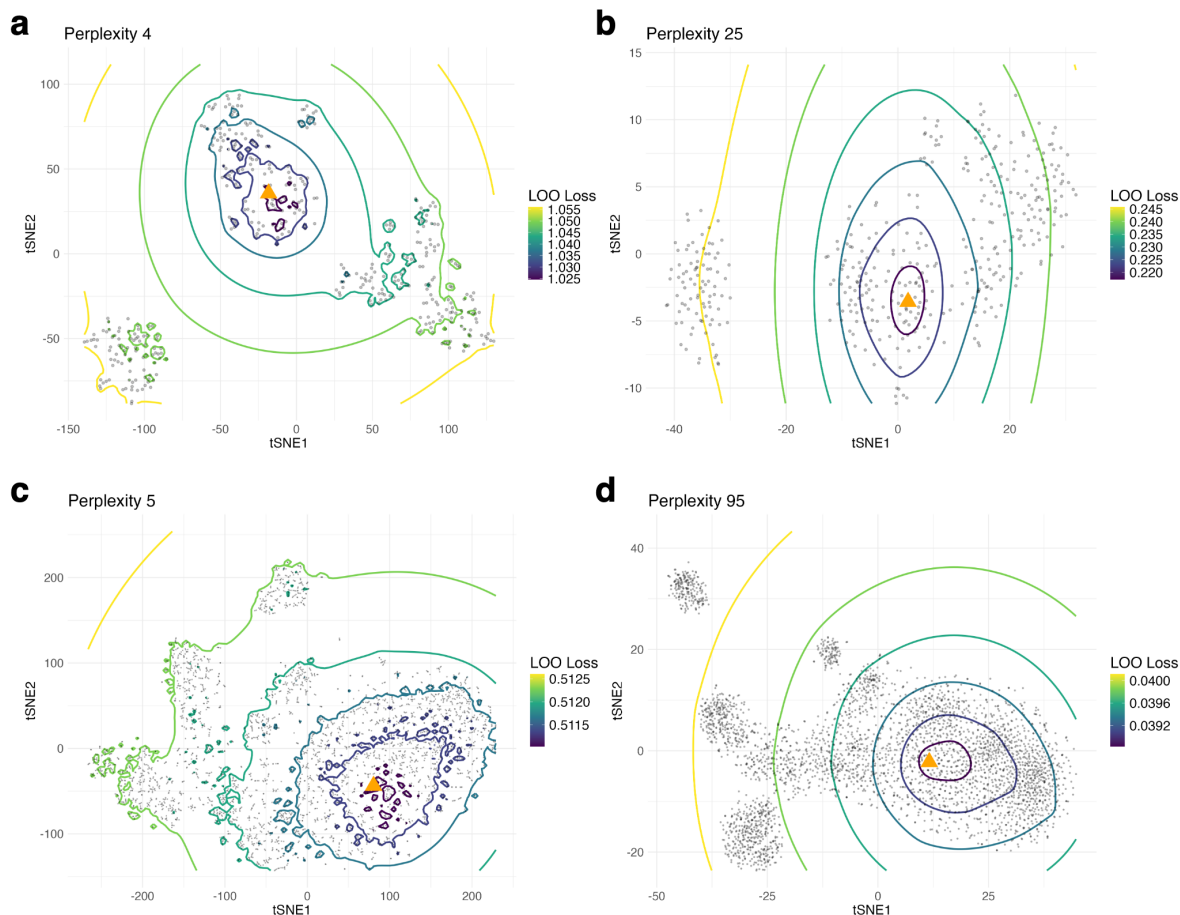


Figure S3: **Comparing loss landscapes for single-cell data with different perplexities.** We present LOO loss landscapes under small and large perplexities for mouse embryonic stem cells differentiation data (**a-b**) and mouse brain single-cell ATAC-seq data (**c-d**). We randomly choose an input x_i from the dataset and plot the landscape of the partial LOO loss $L_i(\mathbf{y}; x_i)$. We observe that more local minima emerge at random locations in the partial LOO loss landscape under a small perplexity than under a large perplexity, which supports our claim about the reduction of local minima and FI discontinuity under a large perplexity.

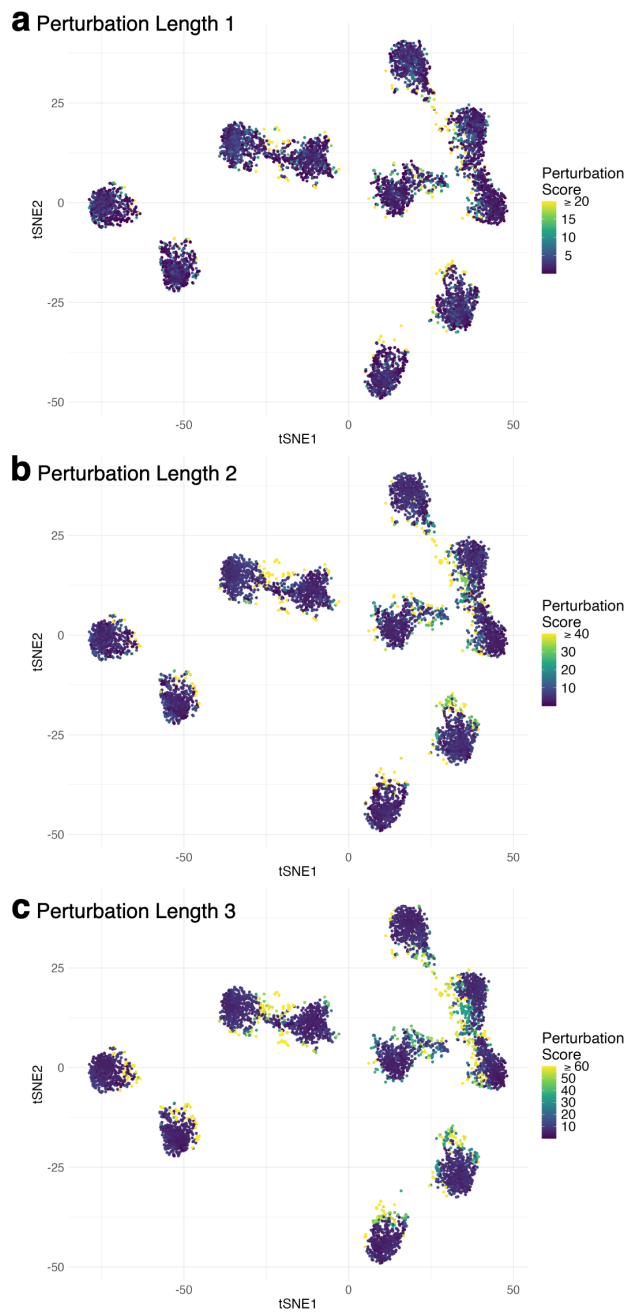


Figure S4: **Perturbation scores of CIFAR-10 image features with different choices of perturbation length.** We vary the choice of the perturbation length $\lambda \in \{1, 2, 3\}$ in the calculation of perturbation scores; see Eqn. 6. We find that embedding points receiving high scores are consistent across different choices of λ . This suggests that perturbation scores are not sensitive to the choice of the perturbation length.

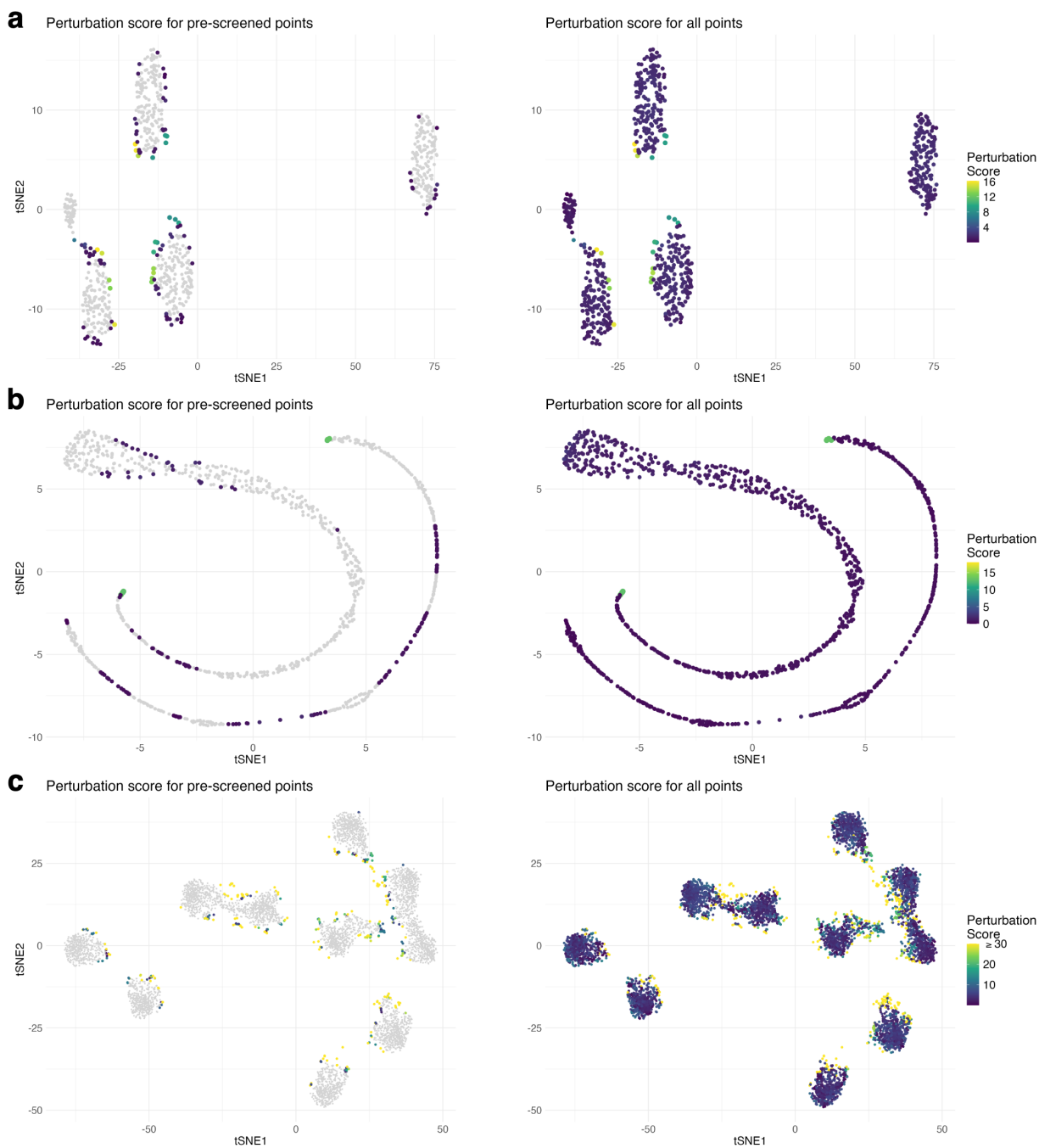


Figure S5: Pre-screening points for calculating perturbations scores provides comparable results. We examine the validity of the pre-screening step by comparing the perturbation scores with the pre-screening step (visualized in left panels) and those without (visualized in right panels). We present the results of perturbation scores on three datasets—5-component Gaussian mixture data (a), Swiss roll data (b), and deep learning feature data of CIFAR-10 (c). We find that the calculating perturbation scores with the pre-screening step still identifies most of the OI discontinuity locations, so pre-screening provides a faster and comparably reliable assessment of OI discontinuity.

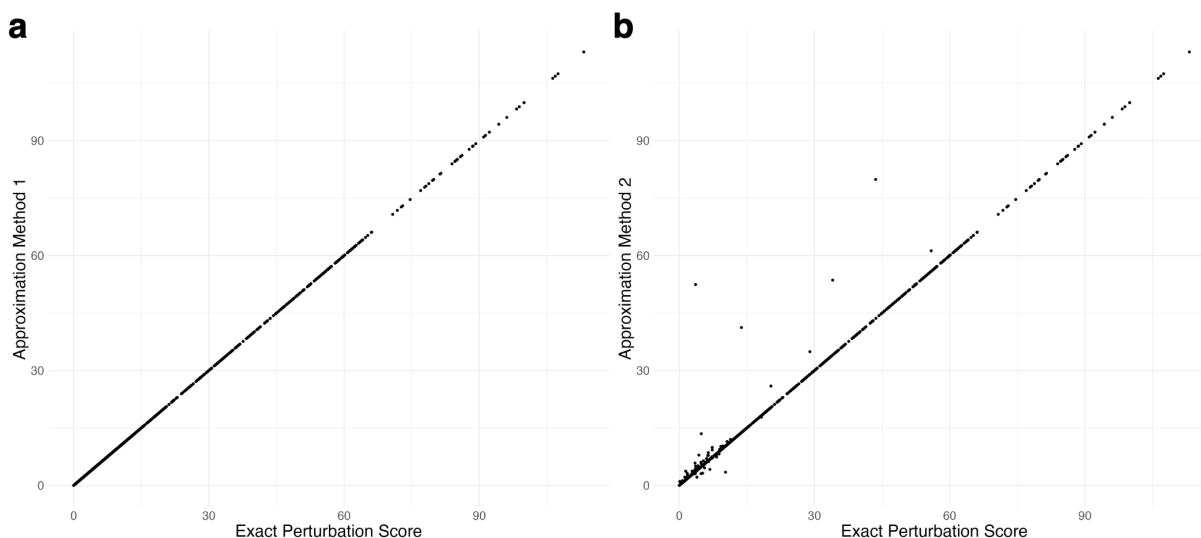


Figure S6: **The approximation method 1&2 are accurate for calculating perturbation scores.** We test the approximation quality on a dataset consisting of 5000 deep learning feature vectors obtained from CIFAR-10 images. **a** Scatter plot of exact perturbation scores v.s. perturbation scores by the approximation method 1. **b** Scatter plot of exact perturbation scores v.s. perturbation scores by approximation method 2. We find that perturbation scores using both approximation methods are approximately equal to the exact perturbation scores for almost all the points.

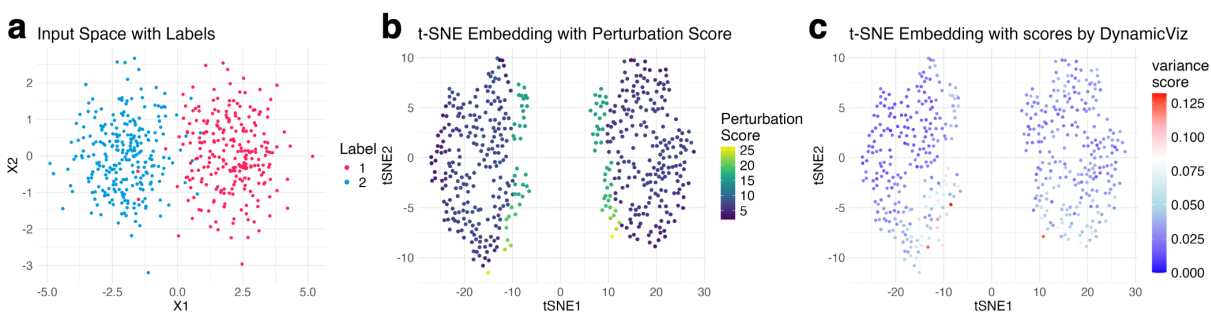


Figure S7: **Comparing perturbation scores and variance scores from DynamicViz.** **a** We use a two-dimensional two-component Gaussian mixture data as the input data. **b** Perturbation scores clearly mark the unreliable embedding points where the disconnection (discontinuity) occurs. **c** DynamicViz fails to identify most of the embedding points that are overconfidently clustered.